Enhanced Photocatalytic and Photovoltaic Performance Arising from Unconventionally Low Donor–Y6 Ratios

Andrew Dolan, Xun Pan, Matthew J. Griffith, Anirudh Sharma, Jessica M. de la Perrelle, Derya Baran, Gregory F. Metha, David M. Huang, Tak W. Kee,* and Mats R. Andersson**

Development of both organic photovoltaics (OPVs) and organic photocatalysts has focused on utilizing the bulk heterojunction (BHJ). The BHJ promotes charge separation and enhances the carrier lifetime, but may give rise to increased charge traps, hindering performance. Here, high photocatalytic and photovoltaic performance is displayed by electron donor–acceptor (D–A) nanoparticles (NPs) and films, using the nonfullerene acceptor Y6 and polymer donor PIDT-T8BT. In contrast to conventional D–A systems, the charge generation in PIDT-T8BT:Y6 NPs is mainly driven by Y6, allowing a high performance even at a low D:A mass ratio of 1:50. The high performance at the low mass ratio is attributed to the amorphous behavior of PIDT-T8BT. Low ratios are generally thought to yield lower efficiency than the more conventional ≈1:1 ratio. However, the OPVs exhibit peak performance at a D:A ratio of 1:5. Similarly the NPs used for photocatalytic hydrogen evolution show peak performance at the 1:6.7 D:A ratio. Interestingly, for the PIDT-T8BT:Y6 system, as the polymer proportion increases, a reduced photocatalytic and photovoltaic performance is observed. The unconventional D:A ratios provide lower recombination losses and increased charge-carrier lifetime with undisrupted ambipolar charge transport in bulk Y6, enabling better performance than conventional ratios. This work reports novel light-harvesting materials in which performance is reduced due to unfavorable morphology as D:A ratios move toward conventional ratios of 1:1.2–1:1.

1. Introduction

The application of organic semiconducting materials for generating renewable energy is constantly growing. Organic photovoltaics (OPVs) offer advantages in the generation of green renewable electricity with desirable properties such as flexibility, light weight, and low processing cost that is associated with a short energy payback time.[1–2] Likewise, organic semiconductors have become desirable in the field of photocatalytic hydrogen evolution thanks to their intense visible light absorption, the lack of which is the primary limitation of their inorganic counterparts. Organic photocatalysis initially used conjugated polymers in combination with metal cocatalysts to provide many of the advantages stated above.[3] Unfortunately, a limitation of these materials was poor excited state and charge carrier lifetime, giving the photocatalysts low efficiency.[4] A solution to the issue of low efficiency was addressed in the field of OPVs.[5] A second component added into the system led to an improved efficiency arising from the formation of

---

A. Dolan, J. M. de la Perrelle, G. F. Metha, D. M. Huang, T. W. Kee
Department of Chemistry
The University of Adelaide
Adelaide 5005, Australia
E-mail: tak.kee@adelaide.edu.au

X. Pan, M. R. Andersson
Flinders Institute for Nanoscale Science and Technology
Flinders University
Bedford Park 5042, Australia
E-mail: caroline.pan@flinders.edu.au; mats.andersson@flinders.edu.au

The ORCID identification number(s) for the author(s) of this article can be found under https://doi.org/10.1002/adma.202309672

DOI: 10.1002/adma.202309672

M. J. Griffith
Future Industries Institute
University of South Australia
Mawson Lakes 5095, Australia

M. J. Griffith
School of Aerospace, Mechanical and Mechatronic Engineering
University of Sydney
Camperdown, NSW 2006, Australia

A. Sharma, D. Baran
Material Science and Engineering Program (MSE), Physical Sciences and Engineering Division (PSE)
King Abdullah University of Science and Technology (KAUST)
Thuwal 23955-6900, Kingdom of Saudi Arabia

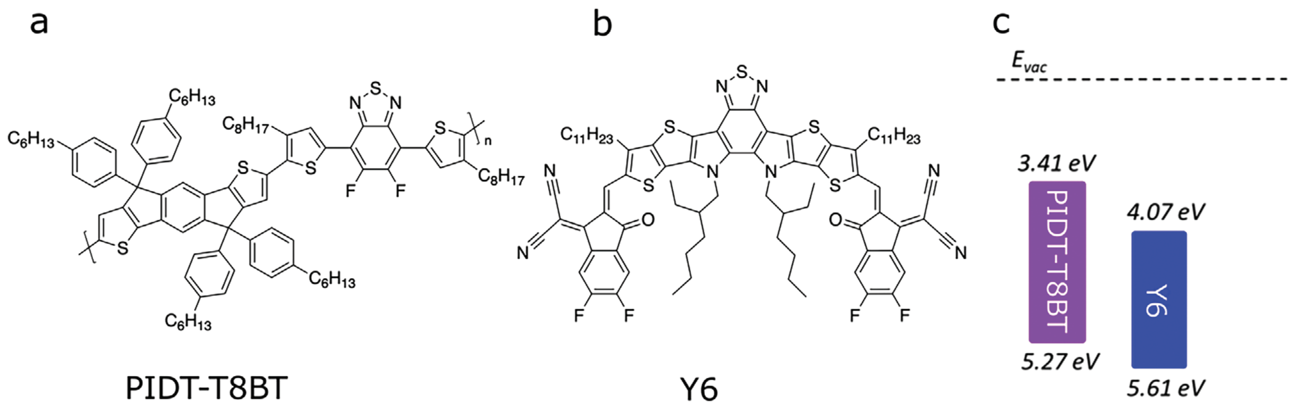

Figure 1. Chemical structures of a) PIDT-T8BT and b) Y6 with c) respective EA and IE energy level schematic. The IE and EA values of PIDT-T8BT were measured using ultraviolet photo-electron spectroscopy and low-energy inverse photoelectron spectroscopy (Supporting Information S2.1 and Figure S2, Supporting Information). The IE and EA values of Y6 were previously reported in literature.[27]

a bulk heterojunction (BHJ). The efficiency improvements brought by the BHJ arose through using an intermixed interlayer of electron donating and accepting semiconductors, referred to as donors and acceptors. At the interface of donor and acceptor domains, an energetic bias due to the differences in the electron affinity (EA) and ionization energy (IE) of the two materials provides a driving force for exciton separation, resulting in spatially resolved charges and limits the effects of recombination. Additionally, the IE and EA also dictate the material's ability to facilitate the oxidation and reduction reactions associated with photocatalytic hydrogen evolution. To facilitate hydrogen evolution from water splitting the donor and acceptor within the BHJ must have an EA less than 4.44 eV and an IE higher than 5.67 eV.[6] However, for blend materials that do not meet those energetic requirements a sacrificial electron donor or acceptor may be used to study either the oxygen or hydrogen evolution reactions. Although the BHJ was a significant factor in improving OPV efficiency, a breakthrough in performance occurred when the field introduced novel fused-ring, nonfullerene acceptors (NFAs),[7–9] which paved the way for the high power conversion efficiency (PCE) values reported today.[10] The combination of the BHJ and NFA materials carried over to the field of organic photocatalysis, with many high-performing hydrogen evolution catalysts being BHJ donor–NFA blends.[11–14]

One of the most prominent molecules that has been used for performance improvements across both OPVs and organic photocatalysis is a NFA known as Y6 (**Figure 1**).[12,15–18] A large component of the success reported by blends incorporating Y6 has been attributed to the material's high charge mobility and generation of free charge in the absence of a donor.[19–20] It was shown by Price et al. that the primary limitation of neat Y6 devices is the rapid rate of charge recombination.[20] In Y6 solid-state films, up to 90% of Y6 excitons dissociate to form free charge, but very few charges live long enough to reach an electrode.[20] This free charge generation in Y6 has led to the material's use as single-component nanoparticle photocatalysts, demonstrating high rates of photocatalytic hydrogen evolution.[17–18] Although the photovoltaic PCE and rates of hydrogen evolution achieved by Y6 as a single-component organic material are impressive, they are outperformed by BHJ materials prepared by blending Y6 with a donor.[12,16,21]

Two recent publications have focused on OPVs prepared with low donor concentration in the blends of PM6 and PTB7-Th with acceptor Y6.[22–23] The PM6:Y6 system achieved over 10% PCE, when the PM6:Y6 ratio in the active layer was 1:10.[22] With a concentration imbalance of donor and acceptor, the bulk properties of the material resembled those of a homojunction as opposed to the BHJ. As shown in the work by Wang et al.,[23] the inherent free charge generation and mobility exhibited by Y6 enabled the use of low concentrations of donor materials to reduce the rate of recombination without significantly disrupting the charge transport channels that can occur in BHJ devices. Reports of Y6 with low donor blends in OPVs are still limited. Hence, the exploration of more donor polymers may elucidate an untapped area of highly efficient OPVs.

PIDT-T8BT was originally developed as a solution-processable electron donor to be paired with small-molecule NFAs.[24] The structure of PIDT-T8BT is shown in Figure 1. This polymer was reported to show a completely amorphous structure as well as a high glass transition temperature of 181 °C. These properties made PIDT-T8BT a potential candidate for organic electronic devices that are resistant to thermal degradation. However, the PIDT-T8BT:Y6 solar cells using the conventional donor:acceptor (D:A) ratio of 1:1.2 only offered modest photovoltaic performance, which discouraged the continued study of this polymer.[24] Inspired by the studies on low donor blends paired with Y6,[22–23] a series of OPVs containing PIDT-T8BT:Y6 over a broad range of D:A ratios were fabricated and investigated for this study. In this work, PIDT-T8BT:Y6 OPVs with a D:A ratio of 1:10 achieved over 10% PCE. Furthermore, 1:50 and 1:25 D:A ratios of PIDT-T8BT:Y6 achieved PCE values of 5.47% and 7.34%, which are the highest reported PCEs for pseudo-homojunction devices specifically at these D:A ratios. To the best of our knowledge, PIDT-T8BT is the first polymer reported that offers higher photovoltaic performance when used in low concentrations with NFA compared to normal BHJ D:A ratios.

Building on the success presented by PIDT-T8BT:Y6 OPVs, this study presents nanoparticles (NPs) of PIDT-T8BT:Y6 blend over a multiple D:A ratios for photocatalytic hydrogen evolution.

As the bend of these materials lacks the required IE to oxidize water (Figure 1d; and Figure S2, Supporting Information) the hydrogen evolution reaction catalyzed by the PIDT-T8BT:Y6 NPs occurred in the presence of sacrificial electron donor ascorbic acid at concentrations consistent with other work in this field.[11–12,14,16–18] It is shown that the success of PIDT-T8BT:Y6 OPVs was mirrored by the NPs, with high rates of hydrogen evolution exhibited by PIDT-T8BT:Y6 NPs with unconventional D:A ratios. Most notably, the pseudo-homojunction PIDT-T8BT:Y6 NPs at a 1:50 D:A ratio outperformed 1:1 PM6:Y6 NPs under the same experimental conditions. Furthermore, the photocatalytic performance continued to increase up to the D:A ratio of 1:6.7. At higher D:A ratios, the rate of hydrogen evolution decreased, resulting in a conventional BHJ blend of 1:1 which performed worse than the materials with a lower D:A ratio, including the neat acceptor. While organic semiconductor NPs with broad ranges of D:A ratios have been reported for photocatalytic hydrogen evolution, performance has been seen to vary greatly across D:A ratios.[11–12,25] This work presents the first example of a unique trend in performance that matches that displayed by the OPVs.

The results of spectroscopic studies of both the solid-state films and NP suspensions indicate the importance of charge generation and mobility in Y6 domains. The excellent charge generation and mobility in Y6 domains which give rise to the high performance exhibited by most other reported donor-Y6 blends remain largely undisrupted in the low-donor blends with PIDT-T8BT:Y6.[26] Our findings reveal the benefit of re-examining existing polymer donors that failed to perform well using a conventional D:A ratio of 1:1.2–1:1. Furthermore, polymers with structural similarity to PIDT-T8BT and amorphous solid state may lead to a library of unexplored high-performance organic photovoltaics and photocatalysts when used in these unconventional D:A ratios.

2. Result and Discussion

2.1. Photovoltaic Device Characterizations

In previous work, PIDT-T8BT showed inferior photovoltaic performances compared to its derivative, PIDT-T12BT.[24] Only a fixed 1:1.2 donor:acceptor ratio was employed in these OPV devices because this previous work focused on understanding the differences in morphology between the two polymer:Y6 blends. By contrast, this study has investigated if the use of lower donor content in the PIDT-T8BT:Y6 system could result in efficient solar devices. Varied PIDT-T8BT:Y6 ratios dissolved in chloroform ($CHCl_3$) were used to fabricate solar cells with an inverted structure of ITO/ZnO/active layer/MoO_3/Ag. Annealing at 150 °C for 10 min was applied to the active layers to promote phase separation without inducing the crystallization of Y6. OPVs with as-cast and annealed active layers were both studied.

First, neat Y6 was used as the active layer, yielding OPVs with a PCE of 0.05%. Thermal annealing of Y6 layer at 150 °C only slightly improved the efficiency up to 0.07%. The low PCE of single-component Y6 OPVs is comparable to previous works reporting conventional device structure and utilizing PEDOT:PSS as the hole transport layer.[20,22–23] However, as an exception neat Y6 OPVs have been reported to reach a PCE of 4.5% when copper(I) thiocyanate (CuSCN) was used as the hole transport layer.[28] With a D:A ratio in PIDT-T8BT:Y6 devices of 1:100, a 2.15% PCE was achieved. Annealing of the active layer at 150 °C improved the PCE to 3.16%, owing to the improved current density (J_{SC}) and fill factor (FF). Further increasing the polymer content to a D:A ratio of 1:50, the devices achieved close to 6% PCE, which outperformed the OPVs with a 1:1 D:A ratio. Functioning OPVs with such a low donor content have rarely been reported, especially when the D:A ratio is less than 1:20.[29] Compared to the PM6:Y6 low donor blend OPVs, which showed 4.78% PCE with 5 wt% donor,[22] our low donor blend OPVs with a similar donor polymer content (1:20 D:A ratio) produced more than 8% PCE from representative cells. The averaged PCE values from cells fabricated using various PIDT-T8BT:Y6 ratios are plotted in **Figure 2a,c**. The detailed device characteristics can be found in Table S1 (Supporting Information). Figure 2a shows that the as-cast PIDT-T8BT:Y6 active layer gave over 10% averaged PCE values when D:A ratios were between 1:5 and 1:3.3. The best-performing cell had an efficiency of 11.2% and was fabricated using a 1:5 D:A ratio.

Thermal annealing of the active layer slightly reduced the open-circuit voltage (V_{OC}) but greatly improved the J_{SC} of devices in all D:A ratios studied in this work, which is attributed to improved phase purity. Specifically, when a 1:3.3 ratio was used, the best-performing cell without annealing showed a PCE of 10.9%, with a J_{SC} of 19.5 mA cm^{-2}, FF of 67.5%, and V_{OC} of 0.83 V. The annealed counterpart achieved J_{SC} of 21.4 mA cm^{-2}, FF of 68.4%, and V_{OC} of 0.81 V, leading to an OPV with a 11.8% PCE, which is the highest among all the devices presented in this work. The external quantum efficiency (EQE) spectrum of the champion cell can be found in Figure S1 (Supporting Information), and the integrated J_{SC} is calculated to be 20.7 mA cm^{-2}. Between 1:5 and 1:2 D:A ratios, the devices with annealed active layers showed similar performance, with over 11% averaged PCE values.

Our results show that thermal annealing had a greater effect on the device performance as the donor content increased. For example, the devices with 1:5 ratio with and without thermal annealing both achieved similar performances. For the 1:2 ratio, however, thermal annealing increased the averaged PCE values from 8.16% to 11.02%, largely owing to the improvement in FF, suggesting a greater balance of charge transport and extraction. We hypothesize that with more donor added to the blend, the as-cast film is likely to have a more disordered, well-mixed phase that may limit charge mobility and promote charge recombination. Since Y6 has long exciton diffusion length (35 nm),[30] thermal annealing may effectively drive the desired phase separation, improving charge transport channels and mitigating the disorder effects. Compared to previously studied polymers in low D:A ratio devices PIDT-T8BT is an amorphous polymer that do not form aggregates in the solid state.[24] This property turns out to be favorable for making high performance devices with low donor content.

Next, we performed dynamic mechanical thermal analysis (DMTA) measurements (Figure S3, Supporting Information) on PIDT-T8BT:Y6 with 1:5 and 1:2 ratios, to establish a correlation between the D/A blend morphology and the device properties. In the case of both ratios before and after thermal annealing, a clear increase of storage modulus (E') was found at ≈200 °C, which is associated with cold-crystallization of Y6 molecules,

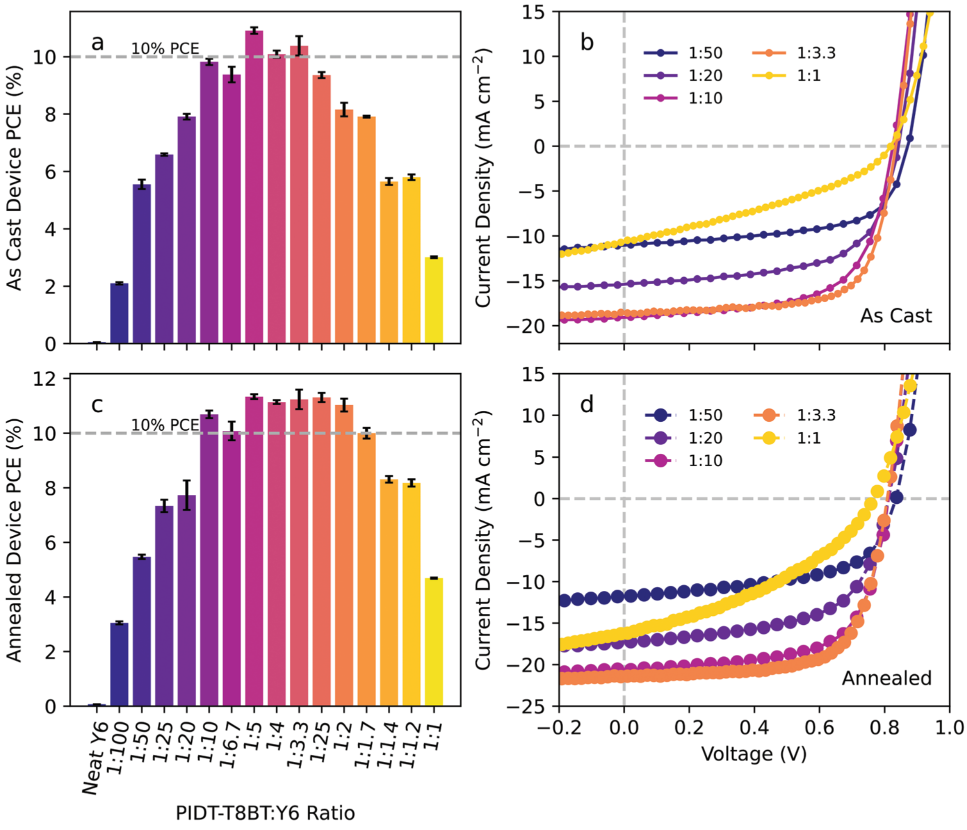

Figure 2. (a, c) Averaged photovoltaic device efficiency for all measured PIDT-T8BT:Y6 blend ratios. Errors bars are twice the standard error of the mean. The PCE of devices is shown a) without annealing and c) with the active layer annealed at 150 °C for 10 min. (b, d) Representative *J*–*V* curves of PIDT-T8BT:Y6 devices using 1:50, 1:20, 1:10, 1:3.3, and 1:1 D:A ratios b) with as-cast active layers and d) with 150 °C annealed active layers.

agreeing with our previous finding.[24] These results also suggest that thermal annealing at 150 °C did not induce large crystal formation in Y6. However, these two blends showed different responses to thermal annealing in terms of phase behavior, indicated by the normalized loss modulus (E'') curves. Specifically, the E'' result for the PIDT-T8BT:Y6 blend with a 1:5 ratio showed a small hump around 170 °C. This E'' hump was accompanied by an E' drop, which is related to the glass transition of PIDT-T8BT-rich phase. This feature in the thermally annealed sample was only marginally enhanced, suggesting that thermal annealing had a minor effect on the phase separation between the two compounds. For the PIDT-T8BT:Y6 blend with a 1:2 ratio, the E'' peak (at ≈170 °C) for the glass transition of PIDT-T8BT-rich phase showed a much narrower feature after thermal annealing, indicating the formation of purer PIDT-T8BT phases as a result of phase separation. To gain a better understanding of the morphological change upon varying the donor content in the blend films and the effect of thermal annealing, atomic force microscopy (AFM) measurements were performed on the PIDT-T8BT:Y6 blend films with D:A ratios of 1:10, 1:5, and 1:1. The AFM height images are shown in Figure S4 (Supporting Information). The as-cast films with 1:10 and 1:5 ratios showed very similar surface features with root mean square (RMS) roughness of 3.32 and 3.33 nm, respectively. Thermal annealing of the 1:10 film resulted in an increase in the RMS value, indicating higher degree of phase separation. The increased phase purity of both donor and acceptor domains is expected to suppress recombination, leading to an improvement in OPV performance. This resulting improvement was observed in the OPV results, where thermal annealing improved the performance of solar cells with 1:10 PIDT-T8BT:Y6 active layer. On the contrary, the 1:5 film showed a slightly lower RMS value after thermal annealing, which agrees with the DMTA results that thermal annealing had a minor effect on improving the phase separation. It is suspected that annealing on the 1:5 film induced a slightly more well-mixed phase, which is reflected by the decreased V_{OC} in the OPVs with annealed 1:5 PIDT-T8BT:Y6 active layer (Table S1, Supporting Information). Finally, the 1:1 PIDT-T8BT:Y6 films showed very homogeneous topographic features and low RMS values for both pristine and annealed compared to those of the films with lower donor content, suggesting the lack of phase separation and a morphology favorable for charge recombination using this normal D:A ratio.

Further increasing the donor content above ratios of 1:1.7 led to deteriorated photovoltaic performances. The 1:1 ratio without annealing only gave a 3.01% averaged PCE, though thermal annealing slightly improved the PCE up to 4.69%. The inferior performance is explained by a lack of phase separation, as shown by the AFM topographic images (Figure S4, Supporting Information). To confirm device performance was not improved with a higher donor content, D:A ratio of 1.5:1 was applied as the active layer, and a very low averaged PCE of 2.10% was obtained (Table

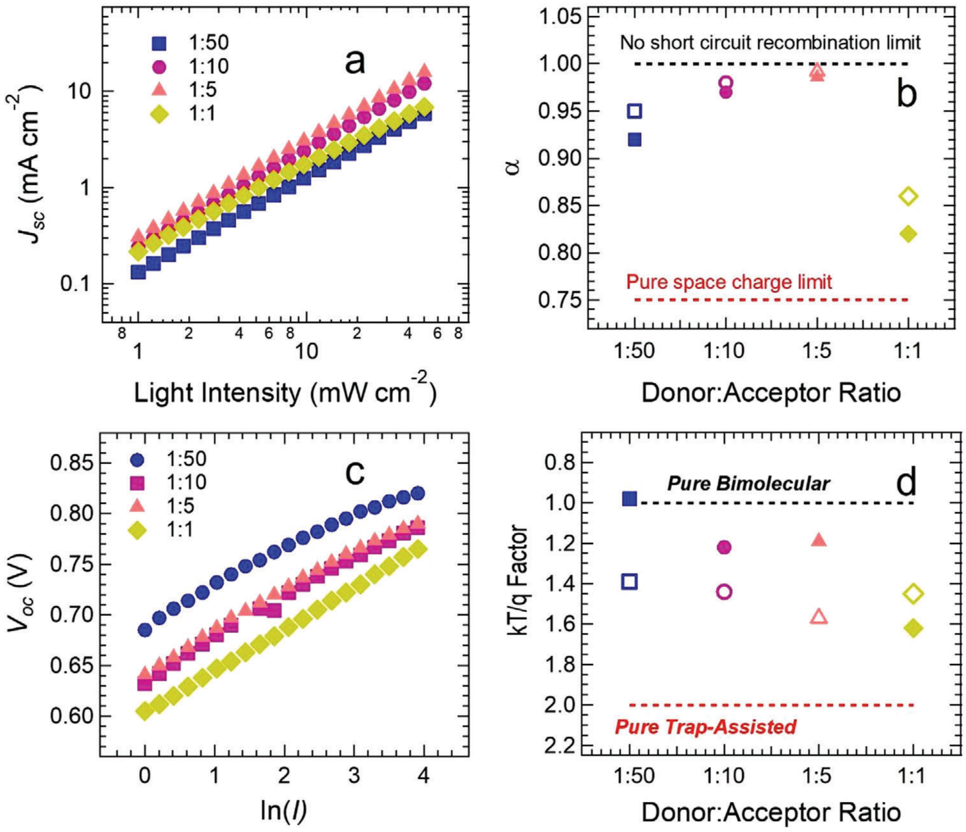

Figure 3. Light intensity dependence of the photovoltaic properties for PIDT-T8BT:Y6 OPV devices with different donor:acceptor ratios. a) J_{SC} versus light intensity for as-cast devices. b) The exponent α extracted from power law fits of the J_{SC} versus I data. c) V_{OC} versus light intensity for as-cast devices. d) The slope of the linear fits to V_{OC} versus $\ln(I)$ plotted as a multiple of kT/q. In (b) and (d), solid symbols represent data for as-cast devices, whereas open symbols show data for thermally annealed devices.

S1, Supporting Information). Representative J–V curves are presented in Figure 2b,d, showing that different D:A ratios largely influenced the J_{SC} and FF, while V_{OC} remained nearly unchanged. The PIDT-T8BT:Y6 blends with unconventionally low D:A ratios offered better OPV performances compared to their BHJ counterparts at a D:A ratio of 1:1.2 or 1:1.

To further develop insights into the dominant charge recombination mechanisms in operating devices, OPVs with PIDT-T8BT:Y6 ratios of 1:50, 1:10, 1:5, and 1:1 were measured under varying light intensities (I = 1–50 mW cm^{-2}). Illumination was applied through a white LED, with intensities modulated by altering the driving current of the diode. The light dependence of the short circuit current has been shown to follow the relationship $J_{SC} \propto I^{\alpha}$, where $\alpha = 1$ is representative of extraction that is not limited by recombination at short circuit, while $\alpha < 1$ can provide insights into the origin of recombination at short circuit.[31–32] **Figure 3a** shows the measured J_{SC} versus I data from the as-cast devices (data from annealed devices are shown in Figure S5a, Supporting Information), with the values of α extracted from power law fits to the J_{SC} versus I data for both as-cast and annealed devices shown in Figure 3b. The as-cast devices show values that systematically increase from 0.92 to 0.99 as more donor content is added from 1:50, 1:10, and 1:5. The 1:1 device then exhibited a significant decrease to 0.82, indicating substantially increased recombination effects at short circuit. After annealing α increased by 1–5% for all four D:A ratios, indicating that annealing improved extraction, reduces recombination, or achieves both at short circuit conditions. The trend in α with respect to the D:A ratio also closely matches the corresponding trends in the device fill factor, implying that the changes in device performance with respect to donor content can be explained by a closer examination of the carrier dynamics. For the 1:1 device, α approached 0.75, which is the value expected when space charge effects are dominant. However, we caution that there can be a range of mechanisms that cause the value of α to deviate from unity, including trap-assisted recombination, bimolecular recombination, nonuniform carrier density distributions in the device, and space charge effects.[33]

To assist in separating these mechanisms, the V_{OC} dependence on light intensity was determined to provide insight into the type of recombination losses that are dominant at open circuit. It has been previously established from the governing photophysics of solar cell devices that the plot of V_{OC} with respect to $\ln(I)$ will be linear, where a slope of $s < kT/q$ indicates surface recombination is the main loss mechanism, a slope of $s = kT/q$ suggests bimolecular recombination dominates, while a slope of $s = 2kT/q$ implies Shockley–Reed–Hall (often referred to as trap-assisted) recombination is the dominant mechanism.[34–35] Figure 3c shows the measured V_{OC} versus $\ln(I)$ data from the as-cast devices (data from annealed devices is shown in Figure S5b, Supporting Information). We note that the plots are not linear across the entire illumination range, and thus analysis of the recombination mechanism has been divided into a "low intensity" regime ($I = 1$–5 mW cm^{-2}) and a "high intensity" regime ($I = 20$–50 mW cm^{-2}). The slopes show values between 1.7 and 1.8kT/q for the low intensity region for the as-cast 1:50, 1:10, and 1:5 devices, decreasing to 1.6kT/q for the 1:1 device (Figure S5c, Supporting Information). This indicates that trap-assisted recombination was dominant at low intensities for these devices, with annealing showing minimal changes for the 1:50, 1:10, and 1:5 devices, although the V_{OC}–ln(I) slope changed significantly to 1.25kT/q for the 1:1 device, indicating an inversion to a bimolecular mechanism dominating recombination at low intensities. The high intensity region, which is more indicative of standard operating conditions and directly comparable to the I–V characterization in Figure 2 and Table S1 (Supporting Information), shows the opposite behavior to what was observed at low intensity. Under higher intensities the V_{OC}–ln(I) slope exhibited values of 0.98, 1.26, and 1.19kT/q for the 1:50, 1:10, and 1:5 devices, respectively, implying bimolecular recombination is dominant in these devices. The 1:1 device in contrast, shows a slope of 1.62kT/q, indicating that trap-assisted recombination starts to become significant at higher light intensities in this device. Annealing of the devices shows the slopes increase to values of 1.38, 1.44, and 1.60kT/q for the 1:50, 1:10, and 1:5 devices, respectively. This increase of the V_{OC}–ln(I) slope after annealing is consistent with trap-assisted recombination becoming more prevalent in the devices. The 1:1 device again showed a different trend, with the slope reducing slightly to 1.45kT/q, though this is still consistent with a combination of bimolecular and trap-assisted recombination influencing the device carrier density at open circuit. The inversion of the dominant recombination loss mechanism from trap-assisted to bimolecular as the light intensity is increased is consistent with findings in previous studies.[36] The emergence of stronger trap-assisted recombination after annealing suggests the creation of defects (structural disorder) or traps due to energetic disorder in the 1:50, 1:10, and 1:5 devices. The 1:1 device already showed significant trap-assisted recombination prior to annealing, suggesting the D:A ratio played a role in increasing the disorder in the system, with low donor content favored in this material system to minimize disorder and maximize performance.

2.2. Photocatalytic Hydrogen Gas Evolution

Many of the highest performing materials used for organic photocatalytic NPs had already displayed high OPV performance when prepared as BHJ films.[11–12,14,16] Hence, the success shown by the low-donor content in the PIDT-T8BT:Y6 OPVs inspired the preparation of NPs with reduced donor content for photocatalytic hydrogen evolution. The NPs were prepared using the miniemulsion method with 2-(3-thienyl)-ethyloxybutylsulfonate (TEBS) as the surfactant and chloroform as the precursor solvent, giving a Z-average diameter between 80 and 120 nm. The similar sizes among these NPs minimizes the influence of NP size on their photocatalytic reaction rates. As shown by the steady-state absorption spectra (Figures S6 and S7, Supporting Information), Y6 is the dominant light absorber. The dominance of Y6 in light absorption is even more pronounced when the donor content is reduced to D:A mass ratios such as 1:50. Y6 has previously been shown to produce free charge as a single component photocatalyst and photovoltaic device.[17–18,20] As well as driving exciton separation through hole transfer,[16] it is anticipated that even under broadband illumination a significant proportion of the charges leading to hydrogen evolution originate from Y6 domains. To enhance comparability between ratios, all photocatalytic hydrogen evolution experiments were conducted at a fixed Y6 concentration of 75 ppm, with an increased D:A ratio only increasing the amount of donor material. This constant Y6 concentration maintained a similar exciton concentration between all the varied ratios. A 2 wt% Pt cocatalyst loading relative to a Y6 mass of 0.225 mg was also used for consistency and comparability between the rates of hydrogen evolution.

Figure 4a displays the average rate of hydrogen evolution by NPs of PIDT-T8BT:Y6 at various D:A mass ratios. The trend in photocatalytic performance shows a 50% increase in the rate of hydrogen evolution with the inclusion of PIDT-T8BT at a 1:50 ratio when compared to neat Y6. The rate continues to increase with the inclusion of more donor material, reaching a maximum at the 1:6.7 ratio, for which the average rate was 6000 ± 200 µmol h^{-1} g^{-1}. The rapid increase in the rate of hydrogen evolution over these ratios reflects what was observed in the OPVs. As the donor content further increases to a more conventional BHJ 1:1 blend, the trend deviates from that displayed by the OPVs. In the NP blend, a significant decrease in rate of hydrogen evolution was observed for the D:A ratio ranging from 1:5 to 1:1, with the 1:1 blend performing worse than NPs of neat Y6. However, as this measure of photocatalyst performance factors in the total mass of material, the reduction in performance exhibited for the higher polymer content ratios may be exaggerated. To address this issue, the EQE, a metric independent of the catalyst mass, was calculated for all D:A ratio NPs as detailed in Section S4.2 (Supporting Information), Table S4 (Supporting Information). The calculated EQEs for all NPs display a trend similar to that shown in Figure 4a, where the 1:6.7 ratio shows the highest performance at an EQE of 0.09%. The trend in EQEs differs from that for the rate of hydrogen evolution after reaching the peak efficiency, where NPs with D:A ratios 1:5 and 1:4 showed a minimal decrease from the maximum efficiency, akin to the PCE results presented in Figure 2.

Figure 4b compares the rate of hydrogen evolution for the D:A ratios of 1:50 and 1:6.7 of PIDT-T8BT:Y6 to that for a conventional BHJ blend of 1:1 PM6:Y6 NPs, which has been shown to be among the best preforming organic photocatalysts to date.[12] Under the same experimental conditions as the PIDT-T8BT:Y6 NPs, the 1:1 PM6:Y6 NPs exhibited an average rate of 4100 ± 300 µmol h^{-1} g^{-1}. The PIDT-T8BT:Y6 system outperformed the 1:1 PM6:Y6 blend not only for the ratios shown in Figure 4b, but also for all blends in which the donor content was at a ratio lower than 1:5. As stated above, Pt loading for hydrogen evolution experiments presented in Figure 4 were all conducted at 2 wt% relative to the Y6 mass. It is well known that increasing the Pt loading leads to increased photocatalytic hydrogen evolution.[11–12,37] To further examine the rate of hydrogen evolution by PIDT-T8BT:Y6 NPs, the 1:6.7 NPs were loaded with Pt at 2 wt% relative to the total mass, which is an increase in the amount of Pt compared to what was used for experiments comparing the different D:A ratios in Figure 4a. The additional Pt loading yielded a rate of hydrogen evolution that is almost identical to that of the 1:1 PM6:Y6 NPs with the same Pt wt%.[16] The comparison of hydrogen

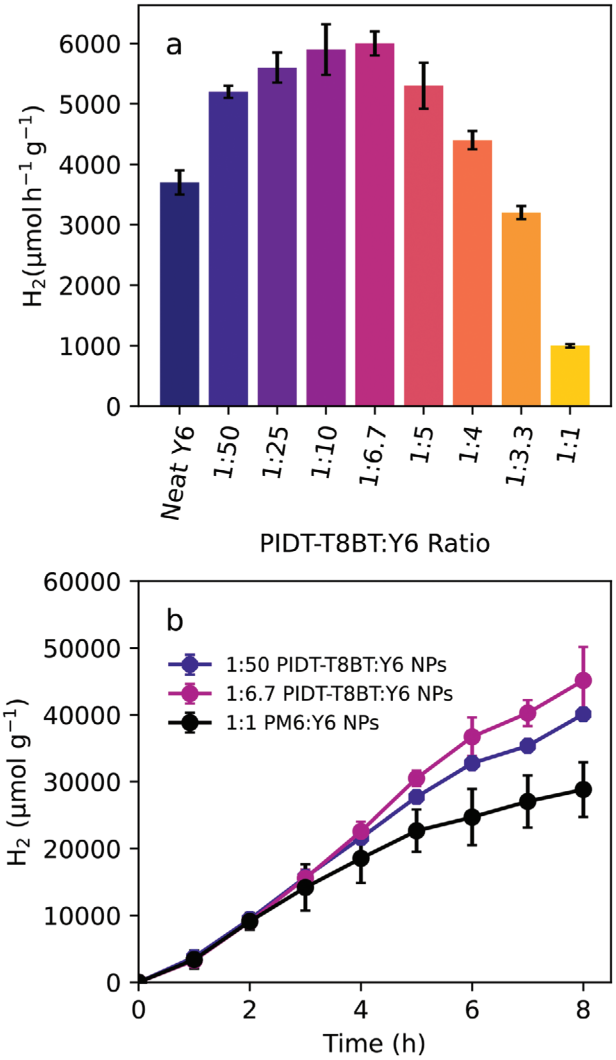

Figure 4. Hydrogen gas evolution by PIDT-T8BT:Y6 and PM6:Y6 NPs at various D:A mass ratios. The values are from triplicate measurements with error bars twice the standard error of the mean. a) Hydrogen evolution rate relative to the total photocatalyst mass for all PIDT-T8BT:Y6 and neat Y6 NPs under identical experimental conditions. b) Hydrogen gas evolved relative to catalyst mass over 8 h reaction period for 1:50 and 1:6.7 PIDT-T8BT:Y6 compared to 1:1 PM6:Y6 NPs with equivalent Pt loading relative to the Y6 mass.

evolution by both the 1:6.7 PIDT-T8BT:Y6 and 1:1 PM6:Y6 NPs at 2 wt% Pt loading relative to total mass can be found in Figure S20 (Supporting Information). The higher performance of the low donor–Y6 blends than conventional donor–acceptor blend ratios (≈1:1) relative to Y6 mass highlights the potential use of low D:A ratios in organic semiconductor NPs. The higher performance indicates a more efficient utilization of charges of Y6 in the low donor-content blends.

2.3. Photophysical Characterization

As discussed above, the blends of PIDT-T8BT:Y6 display a unique trend in both photovoltaic and photocatalytic performance. To better understand this trend in terms of morphology and charge generation, spectroscopic analyses of the PIDT-T8BT:Y6 blends were conducted as a means to determine how the low donor blend ratios outperform the conventional BHJ materials.

2.3.1. Steady-State Spectroscopy

A crucial component of any photovoltaic and photocatalytic material is its steady-state light absorption. This characterization technique not only provides information on the molar absorptivity for the materials but has also been used to understand aggregation behavior.[38] The prevalence of specific aggregate absorption features provides insights into the domain morphology and molecular ordering, both of which impact the material's performance.[38–40] Commonly, the formation of NFA aggregates results in a red shifted absorption spectrum when compared to the equivalent solution spectra, in which the increased lower energy absorption may be attributed to intermolecular electronic interactions.[38]

Figure 5 shows the absorption spectra of neat Y6 and PIDT-T8BT:Y6 at two ratios (1:6.7 and 1:1), prepared as either NPs (Figure 5a) or solid-state films (Figure 5b). The steady-state absorption of solid-state films,Y6 NPs (Figure S9, Supporting Information) and Y6 solution spectrum (Figure S10, Supporting Information) has been compared in previous work.[17] The three solid-state spectra share similarities, with the aggregate peak at 830 nm indicating molecular ordering, and thermal annealing of the solid-state films induced more aggregate peaks between 600 and 800 nm, indicating slightly higher order of Y6 phase. In the case of the NPs, the relative peak height of the aggregate peak to other absorption features is much lower than in films, indicating a more disordered morphology in the NPs. Furthermore, the broad triple-peaked absorption spectrum for the Y6 NPs appears common for NPs formed through either miniemulsion or nanoprecipitation, with the latter process known to produce highly disordered NPs.[12,18,41–42] The changes to the PIDT-T8BT:Y6 blend absorption spectra as a result of increased PIDT-T8BT in the OPV or NP provide insight into the molecular packing of the blend materials.

The progressive change to the steady state absorption of neat Y6 NPs to PIDT-T8BT:Y6 NPs at ratios 1:6.7 and 1:1 is shown in Figure 5a. These two ratios highlight any prominent change for both the low-donor content and BHJ NPs. The absorption spectra for all D:A ratios can be found in Figure S7 in the Supporting Information. Upon the inclusion of PIDT-T8BT, the NP absorption spectrum subtly redshifts, with the most dominant absorption peak occurring at ≈830 nm, opposed to ≈730 nm in the Y6 neat NPs. Along with this redshift, when normalizing to the peak at 730 nm, a relative decrease in the absorption at ≈670 nm was observed. The resulting spectra appear more film-like than that of the original neat Y6 NPs. This redshifted peak absorption cannot occur through any compounding absorptions of the polymer and Y6. Rather, it is likely due to aggregate absorption in the Y6 domains potentially resulting from increased molecular ordering.[38–39]

The molecular ordering of Y6 in the NPs was visible through cryo-transmission electron microscopy (cryo-TEM), with images and corresponding analysis shown in Section S3.3 (Supporting

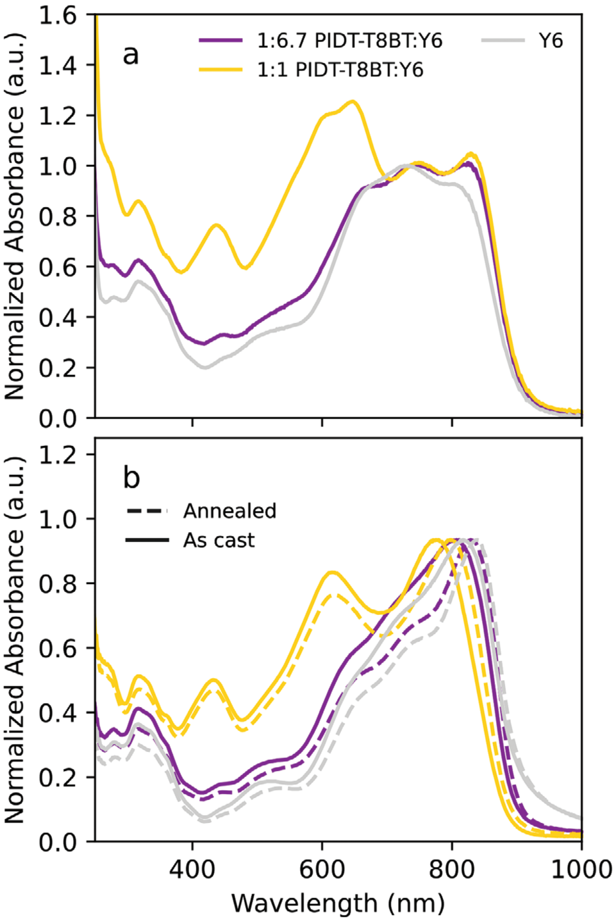

Figure 5. Normalized steady-state absorption spectra of neat Y6, and PIDT-T8BT:Y6 a) NPs and b) films for D:A ratios 1:6.7 and 1:1. The spectra shown for NPs are normalized to the Y6 $S_0 \rightarrow S_1$ absorption at 730 nm,[43–44] while those for the films are normalized to the maximum absorption.

Information). Cryo-TEM images of the 1:1 PIDT-T8BT:Y6 NPs (Figure S13, Supporting Information) revealed a core–shell morphology for the NPs, with Y6 comprising the shell as the imaging showed a lattice structure with a spacing of ≈1.5–2.1 nm similar to that reported for both Y6 NPs and Y6 films as measured by cryo-TEM and grazing incidence wide-angle X-ray scattering (GIWAXS).[12,45–46] The core–shell morphology of the NPs is likely conserved as PIDT-T8BT content is reduced as the cryo-TEM images of the 1:6.7 ratio NPs (Figures S15 and S17, Supporting Information) showed similar features to that of the 1:1 ratio NPs.

After the initial redshift in peak absorption, which can be seen at D:A ratios as low as 1:25 (Figure S7, Supporting Information), the region of the absorption spectra corresponding to Y6 experiences no change. This lack of significant change would be expected for NPs with a core–shell morphology as the two components being restricted to separate domains reduces the impact of electronic coupling between PIDT-T8BT and Y6, as well as changes to molecular packing through the incorporation of more PIDT-T8BT in the NP. The minimal change to steady-state absorption spectra was also observed in the solid-state film spectra (shown in Figure 5b; and Figure S6, Supporting Information). It is hypothesized that this lack of further change to Y6 absorption translates to Y6 domains retaining a high degree of phase purity, allowing efficient charge transport and reducing monomolecular recombination.[20] This hypothesis is supported by the subtle change to the PCE in the low donor-content OPV devices after annealing, a process which enhances phase separation and agrees with the DMTA results presented in Figure S3 (Supporting Information), showing more pure phases of both PIDT-T8BT and Y6 in blend devices after annealing.[47]

Retention of phase purity and decreased miscibility of donor polymers with Y6 have previously been reported to have significant influence on PCE.[48] A donor that is highly miscible with Y6 is P3HT.[48–49] Blends of P3HT and Y6 have been prepared as solid-state films, with OPV performance showing a high dependence on annealing.[48,50] To support the hypothesis that the inclusion of PIDT-T8BT affects the phase purity of Y6 in the blend NPs minimally, 1:1 P3HT:Y6 NPs were prepared through miniemulsion following the same method described in the Supporting Information. The steady-state absorption spectra of P3HT:Y6 (Figure S9, Supporting Information) shows a significant reduction in the absorption peak at 830 nm, suggesting a reduction in the electronic coupling between Y6 molecules. While blends with P3HT reduce the 830 nm absorption, those with PIDT-T8BT did not exhibit this behavior, highlighting the lack of disruption to the morphology of Y6 domains in the PIDT-T8BT:Y6 NPs.

2.3.2. Transient Absorption Spectroscopy

To investigate the mechanisms of charge generation and transport in the PIDT-T8BT:Y6 materials, NPs with D:A mass ratios presented in Figure 4a were probed using transient absorption (TA) spectroscopy. In this study, we focused on only the PIDT-T8BT:Y6 NPs as they displayed a similar performance trend to the solid-state films. Excitation of both donor and acceptor was achieved with either a 400 or 800 nm pump pulse. As the Y6 component was the dominant light absorber for all ratios, it is likely that, for most blends, acceptor excitation provides the best representation of the photovoltaic and photocatalytic photophysics. Hence, **Figure 6** presents the TA data from Y6 excitation, while donor excitation is detailed in Section S5.1 (Supporting Information).

Analysis of the neat NPs was used to assign signals from the donor and acceptor in the blend NPs. TA spectra and power dependence of the neat PIDT-T8BT NPs can be found in Figure S22 (Supporting Information). The polymer shows a ground-state bleach (GSB) from 570 to 690 nm, with features mirroring those of the steady-state absorption,[24] followed by stimulated emission in the range ≈700–800 nm and a strong broad excited-state absorption (ESA) at wavelengths greater than 800 nm. The TA spectrum of Y6 has been studied numerous times over a broad spectral range as NPs and solid-state films, with Y6 GSB in both NPs and solid-state films at 630–890 nm, as well as singlet ESAs at both 480–600 and 900–980 nm.[16–18,20,51–52]

To understand the photocatalytic and photovoltaic performance of the PIDT-T8BT:Y6 blends, we focused on signals that correspond to Y6 free charge. Many studies of Y6 have conducted

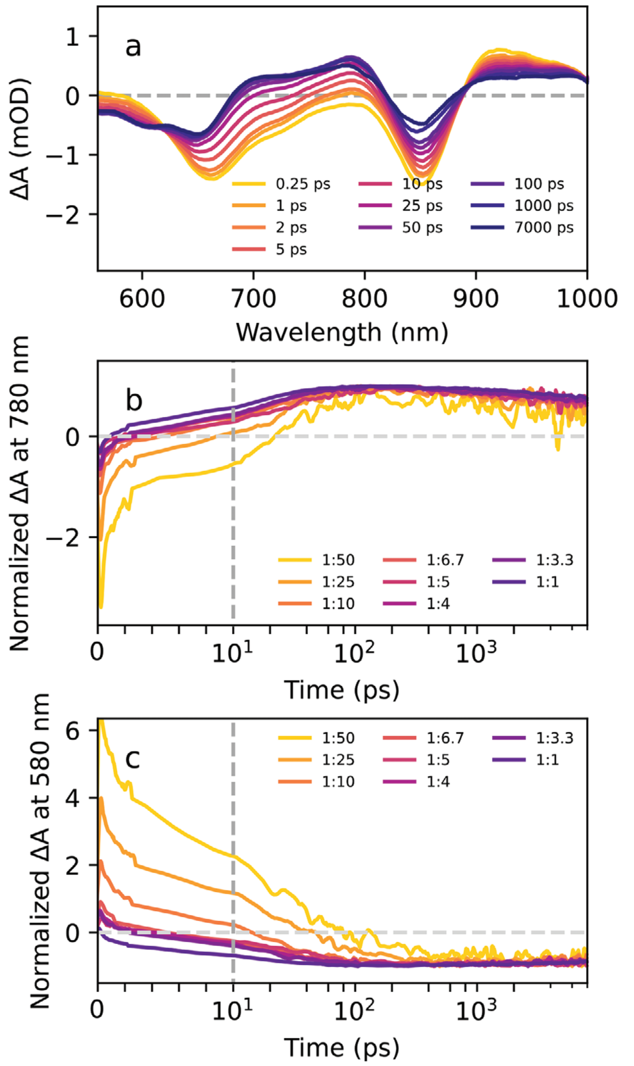

Figure 6. TA spectra and kinetics of PIDT-T8BT:Y6 NPs. a) Spectra for 1:1 PIDT-T8BT NPs excited at 800 nm with a pump fluence of 22 µJ cm^{-2}. The kinetics corresponding to the b) Y6 anion ESA (780 nm), and c) PIDT-T8BT GSB (580 nm) for all PIDT-T8BT:Y6 NPs with the different mass ratios. Kinetic traces in (b) and (c) are normalized to the maximum and minimum signal respectively, which corresponds to when the amount of separated charge is greatest.

spectral assignments using various donors to discern signals associated with charged species.[20,51,53] Two recent works have provided an assignment of the Y6 anion absorption.[20,51] Natsuda et al.[51] assigned two ESAs in the 500–1400 nm spectral region to the Y6 anion: a peak at ≈780 nm overlapping with the Y6 GSB,[51] which has also been reported as an ESA of the charge-separated state in PM6:Y6 films;[53] and broad flat feature between 900 and 1000 nm, overlapping with the Y6 singlet ESA at ≈910 nm.[51–52] The other assignment of the Y6 charge species is from Price et al.,[20] who also assigned the 900–1000 nm signal to charged Y6.[20] Given that both the 780 and 900–1000 nm signal have been assigned as charge, here the 780 and the 910 nm signal have been used to represent the kinetics of Y6 anions. Due to the spectral overlap of Y6 GSB and the 780 nm Y6 anion ESA, the 900–1000 nm ESA signal was selected for best comparison of rates of decay. Although the charge ESA at 910 nm also shares overlap with another absorption being that of singlet excited-state Y6, the spectral contribution is predominantly charge at time greater than 2 ps, due to prompt exciton dissociation within Y6 domains. On the other hand, the conversion of Y6 GSB to Y6 anion ESA at 780 nm best highlights the generation of charge and is presented in Figure 6b.

TA spectra of the 1:1 PIDT-T8BT:Y6 NPs at 800 nm excitation are presented in Figure 6a in the spectral window of 570–1000 nm. The spectral features of the 1:1 PIDT-T8BT:Y6 NPs in Figure 6a are similar to those of blends at other D:A ratios, which are shown in Section S5.2 (Supporting Information). Both the assigned Y6 charge features (780 and 900–1000 nm), as well as spectral contributions from PIDT-T8BT, are evident owing to the high donor content in this blend. At early time after the excitation of Y6 at 800 nm, the PIDT-T8BT:Y6 NPs exhibit a spectral shape reminiscent of neat Y6 NPs presented in previous work,[17] followed by the growth of the Y6 anion ESA at 780 nm, and subsequently the conversion of the Y6 ESA at 580 nm into the PIDT-T8BT GSB. An additional feature that emerges with this shape change is an ESA with a peak at ≈710 nm. Previous work on Y6 has reported a similar ESA feature in donor:Y6 blends, with the absorption ascribed to either a component of the charge-separated state or polymer electro-absorption.[51,53] We have assigned this ESA to an electro-absorption arising from PIDT-T8BT hole polaron generation. This assignment is supported by mirrored kinetics of the growth of the PIDT-T8BT GSB and the 710 nm ESA, shown in Figure S40 (Supporting Information). The growth of the PIDT-T8BT GSB after Y6 excitation at 800 nm can only occur through hole transfer from Y6 to PIDT-T8BT domains, indicating that the mirrored ESA is a result of hole polarons on PIDT-T8BT. Further confirmation of the correlation between the PIDT-T8BT GSB and the 710 nm ESA was achieved through kinetic fitting of the signals, the result of which is shown in Figure S41 (Supporting Information). The similarity in time constants corresponding to the growth of the two signals supports the conclusion that the two signals are correlated and the assignment of the 710 nm ESA to the PIDT-T8BT hole polaron.

The observed shape change in Figure 6a from an initial neat Y6-like spectrum between times of 0.25–1 ps to the spectral shape presented at times after 100 ps is indicative of separated charge due to the persistence of Y6 anion absorption and GSBs for Y6 and PIDT-T8BT. Figure 6b,c shows the TA kinetics at 780 and 580 nm of all NPs, normalized to the maximum signal at 780 nm and minimum signal at 580 nm. The maximum at 780 nm and minimum at 580 nm correspond to the greatest amount of separated charges. The results show that as the polymer content increases, the time taken to reach the maximum amount of free charge is decreased. Correlating this trend to the NP morphology, it is likely that the decrease in time taken to reach the separated charge state occurs through a decrease in the Y6 domain size. Due to the disordered nature of the NPs, changes in long-range ordering of Y6 domains were not observed by steady-state spectroscopy as the short-range molecular aggregates provide the dominant absorption features. However, in the case of the solid-state films, the observed blue shift of the Y6 absorption peak with increasing donor content was likely due to disruption of the long-range ordering with the inclusion of the polymer. The mechanism by which this change to ordering impacts the photocatalytic and photovoltaic performance will be discussed further below.

It is likely that the formation of separated charges on Y6 and PIDT-T8BT occurs through two mechanisms due to the ability of Y6 to generate free charge in absence of a donor.[20] In the first mechanism, a Y6 exciton splits into a free electron and free hole on Y6, which is then followed by the Y6 hole migrating to a PIDT-T8BT:Y6 interface, where the hole transfers to PIDT-T8BT. The second mechanism involves Y6 excitons that are generated a short distance from a PIDT-T8BT:Y6 interface. The exciton can participate in fast hole transfer due to a sizeable difference in IE of the two materials (≈0.3 eV).[24] These two mechanisms can be observed in Figure 6b,c. The initial fast component (< 1 ps) of both the PIDT-T8BT GSB and rise of Y6 anion ESA correspond to rapid interfacial exciton separation. The slower component of PIDT-T8BT GSB growth and Y6 anion ESA rise between 1 and 100 ps show the migration of holes generated in Y6 to PIDT-T8BT. Relating these processes to both photovoltaic and photocatalytic performance, both mechanisms exploit interfacial separation of electron and hole either to promote charge generation or extend carrier lifetime by reducing recombination. However, it is still unclear why the photovoltaic and photocatalytic performance of PIDT-T8BT:Y6 exhibited an optimal performance at D:A ratios ranging from 1:5 to 1:10, for which the D:A interfacial area was less than that of a D:A ratio of ≈1:1.

The most likely explanation for the unusual trend in the performance of the PIDT-T8BT:Y6 blends lies with charge mobility.[20,22] O'Connor et al. established a direct correlation between the charge carrier mobility and the rate of hydrogen evolution in organic photocatalytic NPs,[25] showing that a high-performing photocatalyst must both produce a significant quantity of charge and the charges must have high mobility within the NP. The rate of charge recombination in Y6 has been reported to show a strong power dependence, indicating the Y6 polarons are highly mobile.[20] When Y6 is excited, for all NP blends of PIDT-T8BT:Y6, the TA kinetics remained power dependent (Section S5.2 in the Supporting Information). This power dependence occurred primarily at early times (<100 ps), where the primary excited-state species were Y6 excitons and polarons, with some transfer of holes to the polymer. This early-time power dependence was likely due to bimolecular annihilation of Y6 excitons and polarons, as observed in neat Y6.[17,20] However, on the nanosecond time scale (> 1 ns), the rate of recovery of Y6 ground-state exhibited weak power dependence, as shown in Section S5.2 (Supporting Information). At these times, the excited state population was predominantly charged species spatially separated on PIDT-T8BT and Y6, indicating that the recovery of ground-state Y6 occurred through interfacial recombination, between PIDT-T8BT holes and Y6 electrons. The rate of this interfacial recombination appears first order, indicating dependence on the concentration of only one species. This loss of second order kinetics when progressing from predominantly Y6 polaron recombination to recombination of Y6 electrons and PIDT-T8BT holes implies one of the species has become immobile.

Neat PIDT-T8BT and PIDT-T8BT:Y6 blends exhibited a weak power dependence when the polymer was excited, as is shown in Figures S22 and S23 (Supporting Information). The weak power dependence when PIDT-T8BT was excited indicates that bimolecular recombination of charge carriers originating from the PIDT-T8BT excited state was slow compared to the equivalent process in Y6. As Y6 electrons have been previously shown to be highly mobile, the lack of bimolecular recombination of polymer holes and Y6 electrons suggests poor mobility of polymer holes. These observations indicate that although increasing the PIDT-T8BT content in NPs provides additional interfacial area to promote charge generation, the charges in the PIDT-T8BT domains suffer from low mobility and remain trapped, whereas the charges are highly mobile in Y6.

The photocatalytic reaction requires extraction of holes at the NP surface to oxidize the sacrificial reagent. As discussed above, the mobility of PIDT-T8BT holes is low compared to Y6 electrons, and likely results in holes trapped on the PIDT-T8BT domains. The decreased rate of hydrogen evolution of the 1:1 PIDT-T8BT NPs compared with neat Y6 NPs, was likely a result of a greater proportion of holes within the NP transferred to PIDT-T8BT and no longer being able to migrate to the surface and satisfy the oxidation half of the photocatalytic reaction. However, if all PIDT-T8BT domains acted as hole traps, then it is expected PIDT-T8BT:Y6 NPs at all D:A ratios would suffer from a reduced rate of hydrogen evolution compared to neat Y6 NPs. As discussed above, however, only the 1:1 NPs displayed this reduction in both the quantum efficiency and rate of hydrogen evolution compared to neat Y6 NPs. A plausible explanation that rationalizes the high performance observed in low donor blend ratios and reduced performance at a 1:1 ratio is temporally extended separation of Y6 polarons. Temporal charge separation has been suggested in work by both Price et al. and Wang et al. as a mechanism that may enhance the performance of low donor content Y6 solid-state films.[20,23]

To provide support for the temporal charge-separation mechanism in the PIDT-T8BT:Y6 system, we have considered the kinetics of the Y6 anion ESA, Y6 GSB, and PIDT-T8BT GSB signals. In **Figure** 7a,b, the kinetics of the Y6 GSB (850 nm) and Y6 anion ESA (910 nm) are compared for the PIDT-T8BT:Y6 blend NPs with D:A ratio 1:25 and 1:1 to those of previously studied neat Y6 NPs to highlight the change in excited state species with varying donor concentration. TA kinetics of NPs with other donor concentrations are shown in Figures S42 and S43 (Supporting Information). As noted above, charge recombination kinetics cannot be inferred easily from the decay of the Y6 anion ESA at 780 nm due to spectral overlap with the Y6 GSB. Hence the 910 nm signal was used. For neat Y6 NPs, the recovery of the Y6 GSB in the first 10 ps is significant, decaying to ≈60% of the original signal owing to fast bimolecular recombination (shown graphically in Figure 7c).[17] The rapid recovery of ground-state Y6 is associated with a fast decay in the 910 nm Y6 anion ESA (Figure 7b). During this time, the kinetics associated with this signal are likely due to a decay of singlet Y6 excitons at short times (< 2 ps) and annihilation of Y6 charges at later times (> 2 ps). These kinetics of the neat Y6 NPs are in stark contrast to those for the PIDT-T8BT:Y6 blend NPs, which show very little ground state Y6 recovery, while the 910 nm Y6 anion ESA decays much slower than that of the neat Y6 NPs over the first 10 ps. Additionally, the sharp decay over the first 2 ps observed for the 910 nm ESA in neat Y6 is reduced in the PIDT-T8BT:Y6 blends. The reduced rapid decay in the 910 nm ESA for PIDT-T8BT:Y6 blends shows that a higher proportion of the Y6 excitons dissociated into free charge when

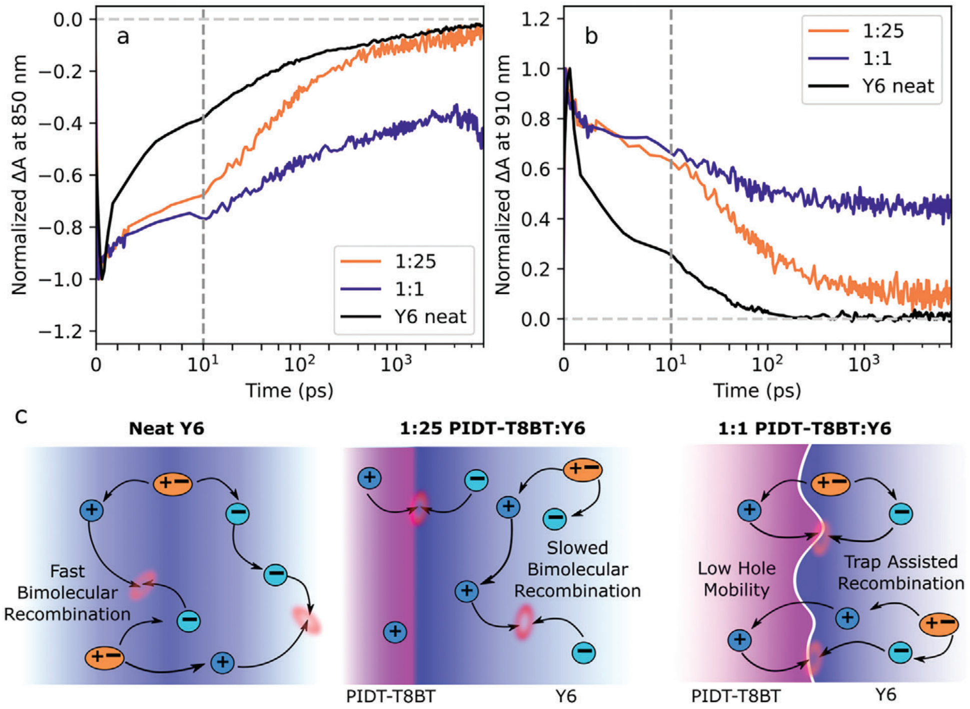

Figure 7. TA kinetics at a) 850 nm and b) 910 nm comparing 1:1 and 1:25 PIDT-T8BT:Y6 NPs with neat Y6 NPs, excited by an 800 nm pump. A pump fluence of 12.5 µJ cm^{-2} was used for PIDT-T8BT:Y6 NPs and 11.2 µJ cm^{-2} for neat Y6 NPs. All signal kinetics are normalized to the maximum signal intensity to highlight the rate of decay. Neat Y6 data were used from previous work.[17] c) Schematic of exciton and charge dynamics inferred from the TA data of neat Y6 and PIDT-T8BT:Y6 NPs at high and low donor content.

PIDT-T8BT was present. During the first 10 ps the TA kinetics of both Y6 GSB (Figure 7a) and Y6 anion (Figure 7b) for the 1:1 and 1:25 PIDT-T8BT:Y6 NPs show vary little difference indicating minimal improvement in exciton dissociation in Y6 through the addition of more PIDT-T8BT beyond the 1:25 ratio, which is further supported by the majority of Y6's fluorescence being quenched at the 1:25 ratio (Figure S12, Supporting Information).

At times between 10 and 500 ps the kinetics of the Y6 anion ESA at 910 nm in the PIDT-T8BT:Y6 blend NPs diverge, with the rate of decay decreasing as PIDT-T8BT content increases. Figure 7b highlights the difference in the 1:25 and 1:1 PIDT-T8BT:Y6 NPs. A comparison of the Y6 anion ESA (910 nm) decay kinetics between D:A ratios 1:50, 1:25, 1:6.7, and 1:1 is shown in Figure S43 (Supporting Information). An increase in polymer content provided a continual decrease in the rate of Y6 electron and Y6 hole recombination. The reduced rate of Y6 charge recombination is largely due to the extraction of Y6 holes onto PIDT-T8BT, the amount of which increased as the D:A ratio approaches 1:1. The higher rate of Y6 anion decay in the low donor-content blends would generally be viewed as a hindrance to the material's photovoltaic and photocatalytic performance. However, this decay exhibited a power dependence, indicating that the kinetics of the excited-state species recombination were largely bimolecular and that these species were mobile. This power-dependent decay was only present in the low donor blends, as shown in Section S5.2 (Supporting Information). Additionally, the time frame over which the power-dependent decay occurred shortened with increasing PIDT-T8BT content, transitioning to a slower power-independent decay. This finding indicates that as the polymer content was increased, the excited-state mobility in the NP was decreased. On the 10–500 ps timescale, the excited species present were predominantly polarons, as shown in Figure 6b, in which the 780 nm anion ESA reaches a maximum for all NP blends by ≈100 ps. Due to the observed maximum in the Y6 anion (780 nm) signal, we can infer that the observed decay in the 910 nm ESA, after ≈100 ps, occurred predominantly via charge recombination. First, bimolecular interfacial recombination between Y6 electrons and PIDT-T8BT holes is considered. If this type of recombination is present the PIDT-T8BT ground state would be expected to recover. As Figure 6c shows, however, the PIDT-T8BT GSB continues to grow during this time frame. Therefore, bimolecular interfacial recombination is unlikely to be responsible for the 910 nm ESA decay. A more likely explanation is the recombination of Y6 electrons and a residual Y6 hole population. This residual Y6 hole population decreased as PIDT-T8BT content was increased, with the increased amount of polymer interfaces extracting more holes from Y6. Although a smaller Y6 hole population enhances the charge carrier lifetime, interfacial recombination of Y6 electron and immobile PIDT-T8BT holes becomes dominant at later times. This result agrees with the recombination mechanisms inferred by the light intensity OPV measurements, and highlights that the increased donor content reduces the amount of charge that may be extracted in either the OPVs or photocatalyst leading to the poor performance in high donor-content blends.

Relating the TA data to the PIDT-T8BT:Y6 OPV and NPs photocatalytic performance, the inclusion of PIDT-T8BT enhances charge generation and slows charge recombination. The slow recombination is due to a temporal separation of electrons and hole onto Y6 and PIDT-T8BT domains, respectively. This enhancement in both the quantity of charges generated and the charge carrier lifetime provided by the addition of PIDT-T8BT resulted in the performance increase of PIDT-T8BT:Y6 blends relative to neat Y6. On the other hand, the peak OPV and photocatalyst performance for a relatively low donor-content blend is explained by minimal improvement in charge generation for D:A ratios where PIDT-T8BT to Y6 content is above a 1:25 mass ratio, and by low charge mobility in donor domains, which enhances charge recombination at donor–acceptor interfaces and diminishes charge extraction. Figure 7c illustrates this explanation of the OPV and photocatalyst performance of the PIDT-T8BT:Y6 blend ratio. Although our TA measurements showed an increased charge carrier lifetime at higher donor content blends, the charge mobility was significantly slowed. Most charges are extracted in OPV devices on the microsecond or longer time scale, which was not probed in the TA spectroscopy experiments.[54] It is likely that the reduced mobility of charges in the high donor content PIDT-T8BT blends leads to a greater rate of charge recombination on longer time scales compared to that of the low donor blends where the charges have higher mobility. Additionally, higher charge mobility has been shown to reduce the time taken for charges to be extracted,[54] meaning the low donor blends may be less affected by long time charge recombination. Hence, the longer charge carrier lifetime where the charges have low mobility plays a negligible role in OPV or photocatalytic performance.

Furthering the spectroscopic insight into the photocatalytic performance by PIDT-T8BT:Y6 NPs, TA spectroscopy of the 1:6.7 and 1:1 D:A ratio NPs was conducted under photocatalytic conditions. A detailed description of the experimental procedure and results can be found in Section S5.5 (Supporting Information). The impact of the photocatalytic conditions on the PIDT-T8BT:Y6 NPs excited-state kinetics in both the 1:1 and 1:6.7 D:A ratio NPs were minor due to TA spectroscopy probing bulk properties and therefore being insensitive to surface processes that would be most affected by the catalysis conditions. Signals corresponding to the Y6 anion (910 nm) and PIDT-T8BT GSB (580 nm) showed subtle differences in kinetics on the nanosecond time scale, with the 910 nm signal exhibiting a greater rate of decay (Figures S45b and S47b, Supporting Information) owing to extraction of Y6 polarons by the Pt cocatalyst. As for the PIDT-T8BT GSB, the presence of Pt and ascorbic acid reduces the signal intensity of the GSB at 580 nm, implying a reduction of PIDT-T8BT holes. Normalizing to the signal intensity at 1 ns showed minimal change to the rate of decay in the 580 nm signal over the remaining 7 ns, as shown in Figures S44a and S46a of the Supporting Information. Due to the core–shell NP morphology it is most likely that the reduced yield of PIDT-T8BT holes was due to quenching of Y6 holes prior transfer to PIDT-T8BT domains, and any quenching of the PIDT-T8BT holes arose through recombination with Y6 electrons as opposed to the oxidation of ascorbic acid. In general, the experiments indicate that all reductive and oxidative reactions were driven by charges present on Y6 domains. Further analysis into the changed TA kinetics is detailed in Section S5.5 (Supporting Information).

The proposal that poor charge mobility in high donor content blends limits device performance is supported by the changes in the FF discussed in Section 2.1. Figure 2 shows that annealing of the OPV devices with a higher donor content led to more significant improvement of both the PCE and FF than that for a lower donor content, where Figure 3b highlights that recombination at short circuit was reduced after annealing the active layers in these devices and the influence of trap-assisted recombination became lower, with bimolecular recombination becoming more dominant. Each of these results is consistent with a hypothesis that annealing improved the balance in charge transport and extraction as a result of morphological changes in PIDT-T8BT and Y6 domains for devices with higher donor content.[24] A balance in charge transport and extraction was achieved in devices with low donor content due to the retained Y6 hole population having high mobility and extended carrier lifetime compared with neat Y6. Furthermore, in the photocatalytic reaction, only a small fraction of the incident photons resulted in the evolution of hydrogen, as indicated by the EQEs described in Section S4.2 (Supporting Information). Hence, it is likely the residual population of mobile Y6 holes present in the low donor content NPs was sufficient to catalyze the oxidation of the sacrificial reagent, and the increased charge carrier lifetime provided the increased performance comparatively to neat Y6. This result highlights the importance of balanced charge carrier lifetime and charge mobility for both OPVs and organic photocatalysts.

2.3.3. Transient Electrical Measurements of Carrier Dynamics in Operating Devices

To test the hypothesis presented at the end of the previous section further, the charge carrier dynamics (mobility and lifetime) were probed further using transient electrical techniques. First, the charge carrier mobility was determined in OPV devices fabricated with D:A ratios of 1:50, 1:10, 1:5, and 1:1 using the photoCELIV technique as described in Section S6 (Supporting Information). Current traces were measured at multiple different light intensities (Figure S48, Supporting Information), with full extraction of photogenerated carriers under the applied voltage ramp verified by the return of the current trace back to the dark geometric capacitive current for all devices and intensities measured. Carrier mobilities were extracted from the current traces using the intermediate conductivity regime equation that has been widely applied to organic photovoltaic devices.[55] Mobilities were found to be slightly higher in the low intensity regime (I = 1–5 mW cm^{-2}), but the mobility stabilized at a constant value in the high light intensity regime where OPV devices were tested (I = 20–50 mW cm^{-2}). The current traces at the highest light intensity are shown for as-cast devices in **Figure 8**a, while stabilized mobility values for both as-cast and annealed devices are shown in Figure 8b for each of the different D:A ratios. The carrier mobility determined by photoCELIV was found to systematically increase with the addition of increased concentrations of PIDT-T8BT in the blends with Y6, from a value of (1.4 ± 0.2) × 10^{-5} cm^2 v^{-1} s^{-1} for the 1:50 device to (3.3 ± 0.7) × 10^{-4} cm^2 v^{-1} s^{-1} for the 1:1 device. This trend remained constant in both the as-cast and annealed devices, though the annealed devices exhibited a consistent increase in carrier mobility of between 10% and 40% compared to the as-cast devices. The mobility determined by photoCELIV represents an ambipolar value, which is the mean

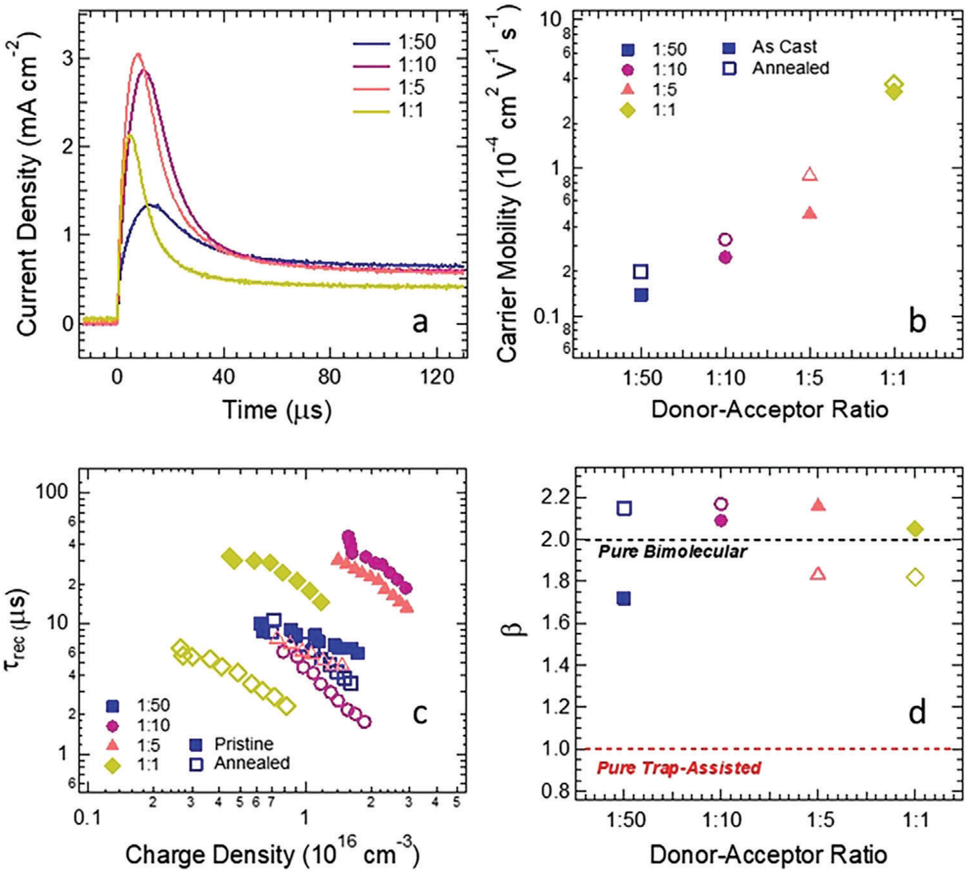

Figure 8. Measurements of charge carrier dynamics for PIDT-T8BT:Y6 OPV devices with differing donor acceptor ratios. a) PhotoCELIV current transients for as-cast devices at the highest light intensity (≈50 mW cm^{-2}). b) Carrier mobility extracted from photoCELIV current transients. c) Corrected recombination lifetimes determined from the TPV decay time constants representing the bulk recombination lifetime (τ_{rec}) as a function of carrier density in the film determined by TRCE measurements. d) Recombination order of devices determined from the slope of τ_{rec} versus carrier density (n) plots. Theoretical values for pure trap-assisted (red) and pure bimolecular (black) recombination mechanisms are shown as dashed lines. In (b) and (d), solid symbols represent data for as-cast devices, whereas open symbols show data for annealed devices.

of the electron and hole mobilities scaled by their relative carrier concentrations. Accordingly, the fastest carrier is expected to dominate the mobility value measured using the photoCELIV technique. Previous studies of the Y6 system have shown it is ambipolar, with the mobility of electrons reported to be a factor of 2–3 times greater than that of holes in intrinsic Y6-only devices.[22,56] Both the Y6 hole mobility reported in these studies and the PIDT-T8BT hole mobility reported in our previous work are lower than the maximum carrier mobility determined in this work,[24] leading us to assign the mobility measured by photoCELIV to electron transport in Y6. To rationalize why this mobility increased by more than an order of magnitude as the D:A ratio was increased from the 1:50 to the 1:1, we consider both the complex nature of charge generation and recombination revealed by the TA measurements in this work and the data and interpretations reported in previous studies of low donor-content devices with Y6 as an electron acceptor. The TA measurements revealed that addition of PIDT-T8BT resulted in extraction of holes from the ambipolar Y6 via transfer to PIDT-T8BT. This hole transfer process reduced the fast nongeminate recombination occurring between free charges generated by excitation of the Y6, a process that would be expected to systematically increase the electron mobility inside the Y6 as the amount of PIDT-T8BT is increased, exactly as was measured in the mobility data in Figure 8b.

To verify that the recombination of carriers in OPV devices is consistent with the above proposed device photophysics, the carrier lifetime was measured using transient photovoltage (TPV; voltage traces shown in Figure S49, Supporting Information) and the carrier density was determined using time-resolved charge extraction measurements (TRCE; current traces shown in Figure S50, Supporting Information). The carrier lifetime provides information on the recombination kinetics, although we note that there have been several recent reports that advise careful consideration of device properties when utilizing the time constant of TPV decay to assess bulk recombination, since the measured photovoltage decay has also been shown to be related to the accumulation and recombination of charge in the space-charge regions at the absorber–transport layer interfaces and/or capacitive effects within the device.[57–58] In such cases, the evolution of photogenerated carriers producing the TPV signal can be dominated by properties such as the mobility or relative permittivity of photoactive materials, the bias light intensity, and the device capacitance. Accordingly, we have corrected the native time constants extracted from the TPV decays (τ_{TPV}) using the quantitative approach reported by Krückemeier et al. that considers the native TPV decay time, the capacitive and photogenerated charge carrier densities (measured by TRCE) and the exchange velocity in the devices due to current flow to and from the electrodes to obtain the bulk recombination lifetime (τ_{rec}).[59] The values of the recombination lifetimes are plotted against the extracted photogenerated carrier density inside devices in Figure 8c. By comparing devices at a matched carrier density to remove the influence of carrier density on recombination, it is clear that the lifetime in devices with D:A ratios of 1:10 and 1:5 was higher than that in the 1:50 device by approximately an order of magnitude for as-cast devices, whereas the lifetime was reduced in the 1:1 ratio device to a value ≈2 times higher than the 1:50 devices. The annealed devices showed approximately equivalent carrier lifetimes for the 1:50, 1:10, and 1:5 devices, with a significantly lower lifetime in the 1:1 device. These measurements suggest that the recombination is reduced as the D:A ratio is increased from 1:50 to 1:10 and 1:5, but then becomes significantly faster with a continued increase in the D:A ratio to 1:1. The recombination mechanism was extracted by analyzing the slope of the τ_{rec} versus carrier density (n) plots, since it has been shown that the reaction order for recombination (β) is given by

$$\beta = 1 + \frac{\mathrm{d}\ln\tau^{-1}}{\mathrm{d}\ln n} \tag{1}$$

The values of β are plotted for as-cast and annealed devices prepared from the four different D:A ratios in Figure 8d, where predicted values for pure trap-assisted ($\beta = 1$) and pure bimolecular recombination ($\beta = 2$) are also indicated. The values of β are close to 2 for all the as-cast devices, suggesting bimolecular recombination is dominant in these devices. This is consistent with the interpretation of recombination order from the V_{OC} dependence on light intensity in Figure 3d, with the exception of the 1:1 device, which showed more significant trap-assisted recombination in the V_{OC} versus ln(I) analysis than the τ_{rec} versus n analysis. Annealing the active layer in the devices induced minor changes for the 1:50 and 1:10 devices. However, the 1:5 and 1:1 devices showed a decrease in β that indicates the emergence of stronger trap-assisted recombination, though the overall order still remained closer to 2 than 1 (≈1.8) in these devices. Again, this result is consistent with that obtained earlier in the V_{OC} versus ln(I) measurements.

The carrier mobility and lifetime results are consistent with both the steady state light intensity dependence analysis and the TA measurements, and confirm the mechanism for the peak in performance of device occurring at a ratio significantly lower than 1:1. The addition of PIDT-T8BT to Y6 assist with charge generation and removes holes from the Y6 into the PIDT-T8BT, which enables the electron mobility in Y6 to increase and the recombination between free electrons and holes in Y6 to decrease. As has been noted in previous studies, the donor material in low-donor devices with Y6, including PM6 and PTB7-Th often acts as a significant hole trap, which is consistent with the low mobility of holes proposed from the transient absorption data and the observed increased recombination rate and change to a more dominant trap-assisted recombination order observed in the 1:1 devices, in which hole traps become prevalent.[20,22–23] The low fill factor in 1:1 devices and the value of α significantly lower than unity in the J_{SC} versus I data in Figure 3b also support unbalanced carrier mobility in the 1:1 device, leading to space charge effects (or similar extraction limitations on the photocurrent) at this D:A ratio. The unique insight in this work that the 1:1 D:A ratio is not the performance maximum may arise from the use of a completely amorphous donor material with significant disorder in the pristine state, which shifts the transition between the competing benefits of improved electron mobility and charge generation and limitations of enhanced recombination and reduced hole mobility due to addition of the donor to much lower donor ratios than have been previously observed. Excitingly, these findings imply that polymers with structural similarity to PIDT-T8BT and an amorphous solid state may represent a significant new library of unexplored materials to create new high performance organic photovoltaics and photocatalysts when used in these unconventional D:A ratios.

3. Conclusion

Using the recently reported amorphous donor polymer PIDT-T8BT in conjunction with the high performing NFA Y6 at low donor D:A mass ratios, solar cells with over 10% PCE were fabricated. The high PCE was only exhibited when the D:A ratio was between 1:10 and 1:2, likely due to the amorphous nature of PIDT-T8BT. Additionally, a D:A ratio of 1:50 gave functioning photovoltaic devices with 5.93% PCE, while OPVs with a ratio of 1:5 achieved over 11% PCE. The investigation on the OPVs with varied donor content reveals that low donor blends with D:A ratios of 1:10 and 1:5 offered lower recombination loss as well as higher charge carrier lifetime compared to that of tradition 1:1 ratio. At high donor contents the blend morphology is not optimal due to residual amorphous polymer in the Y6 domains. A detailed photocatalytic study of nanoparticles made from PIDT-T8BT:Y6 revealed a similar performance trend to the OPVs. High rates of hydrogen evolution were exhibited by low donor blend ratios, with a D:A ratio of 1:6.7 achieving the highest rate at 6000 ± 200 µmol $\mathrm{h^{-1}\ g^{-1}}$. Impressively, low donor blends with D:A ratios between 1:50 and 1:5 outperformed 1:1 PM6:Y6 nanoparticles, one of the best-performing organic hydrogen-evolution photocatalysts reported thus far. The high photovoltaic and photocatalytic activity presented by low donor blends of PIDT-T8BT:Y6 is largely attributed to reduced rates of charge recombination in Y6 domains through limited hole extraction onto PIDT-T8BT. Additionally, the decreased performance displayed as the donor–acceptor ratios approach more conventional ratios such as 1:1 and 1:1.2 was rationalized by low charge mobility due to nonoptimal morphology leading to trap-assisted recombination.

Moreover, long-range ambipolar charge transport pathways in Y6 are crucial for high activity in both applications, as an increased polymer concentration results in a reduction in overall performance. Although several reports have shown high performance in OPVs fabricated with low donor blend ratios, this work is the first to show a correlation between the OPV performance of such solid-state films and photocatalytic activity of the corresponding NPs. Additionally, to our knowledge this is the first reported donor–acceptor system to achieve better OPV performance in unconventionally low donor blend ratios compared with the conventional 1:1.2 ratio and this performance trend may be related to the amorphous nature of the PIDT-T8BT. This work highlights the use of a low donor content to enhance the performance of organic semiconducting materials and demonstrates the performance correlation between OPVs and organic photocatalysts.

4. Experimental Section

Materials: The solvents used in this work were sourced from Sigma-Aldrich and used without further purification. Y6 used to fabricate OPVs was purchased from SunaTech Inc. PIDT-T8BT was synthesized according to reported procedure.[24] The molecular weight was determined using high temperature GPC with 1,2,4-trichlorobenzene as eluent, giving a $\bar{M}_n$ of 62.4 kg mol^{-1} and a $Đ_M$ of 2.59. PM6 ($\bar{M}_n$ 37.3 kg mol^{-1}, $Đ_M$ 2.92) and Y6 used in NP synthesis were purchased from Ossila and used without further purification. The surfactant TEBS was purchased from Solaris and water was purified using an 18 MΩ Millipore Milli-Q reagent water system with a 0.45 µm filter. Photodeposition of Pt NPs was achieved using chloroplatanic acid hexahydrate (K_2PtCl_6), purchased from Sigma-Aldrich (CAS no. 97-13-7). L-Ascorbic acid (99%) was purchased from Chem Supply.

Photovoltaic Device Preparation: Inverted solar cells with the structure ITO/ZnO/active layer/MoO_3/Ag were fabricated using different mass ratios of PIDT-T8BT:Y6 in the active layer. PIDT-T8BT and Y6 were dissolved together in $CHCl_3$ in a nitrogen protected glove-box overnight prior to the active layer deposition. Thermal annealing of the active layer was conducted in a nitrogen protected glove-box on a hotplate. The reported annealing temperatures were the temperatures displayed by the thermocouple of the hotplate. Further details are in Section S1 (Supporting Information).

Photovoltaic Device Characterization: Photovoltaic properties of solar cells were measured in air by an Oriel solar simulator fitted with a 150 W xenon lamp (Newport). The lamp output was filtered to give an irradiation of 100 mW cm^{-2} at an atmospheric mass (AM) of 1.5 and calibrated using a silicon reference cell with NIST traceable certification. The photocurrent–voltage (I–V) characteristics of the devices were measured through a Keithley 2450 source meter unit.

Atomic Force Microscopy (AFM) measurements: AFM instrument was supplied by Bruker, Billerica, MA. The measurements were performed in tapping mode using silicon tips. The AFM samples were prepared by spin-coating from the same solutions used for device fabrication, on freshly cleaned ITO-coated glass substrates.

Photocatalytic Hydrogen Evolution Reaction: Photocatalytic evolution of hydrogen gas by all organic semiconducting NPs was achieved using the sacrificial electron donor ascorbic acid, and platinum (Pt) as a cocatalyst. To assess the effect of PIDT-T8BT concentration on hydrogen gas evolution, experiments were conducted with all NP ratios maintaining a Y6 concentration of 75 ppm with a Pt loading at 2 wt% of the Y6 mass.

The suspension of NPs in water (3 mL) with sacrificial reagent ascorbic acid (0.2 M) and K_2PtCl_6 solution (140 µL, 80 ppm) was added to a liquid batch reactor (13 mL volume, 1.77 cm^2 top-down illumination area). Overhead illumination of sample by a Xe arc lamp (300 W, Stryker X6000) at solar intensity (100 mW cm^{-2}) facilitated in situ photodeposition of Pt and hydrogen gas evolution. Prior to each reaction, air was evacuated and replaced with argon gas at atmospheric pressure. The reaction was stirred continuously, and 500 µL of gaseous product was sampled hourly with 400 µL externally injected into a gas chromatograph (Agilent 7890B GC, argon carrier gas).

Steady-State Spectroscopy: Steady-state absorption of films was characterized using Agilent Cary 60. Neat Y6 films and PIDT-T8BT:Y6 films were spin-coated from the same solutions used for the deposition of solar cell active layer at 2000 rpm for 1 min on cleaned glass slides. Thermal annealing was conducted on a preheated hotplate at 150 °C in air after the measurement of as-cast films.

Steady-state UV–visible absorption and emission of NPs were obtained using a Cary 3500 Compact UV–Vis spectrophotometer and PS Shimadzu RF-6000 fluorescence spectrophotometer, respectively. Samples were loaded into a 1 cm path length quartz cuvette (Starna cells 21-Q-10).

Transmission Electron Microscopy: Cryo-TEM experiments were conducted with NP samples deposited from an aqueous suspension onto carbon lacey film coated TEM grids (TEMLC200U100) and evaporated to dryness. Grids were then flash frozen in liquid nitrogen and images were collected with a ThermoFisher Scientific Glacios 2 Cryo-TEM with operating voltage of 200 kV.

Transient Absorption Spectroscopy: TA spectroscopy experiments were performed using a home-built TA spectrometer. Pump pulses of 800 and 400 nm with ≈230 fs instrument response time were generated using a home-built optical parametric amplifier (OPA) pumped with a 1030 nm pulsed laser (Light Conversion, Pharos). Probe pulses were generated by focusing the 1030 nm output onto a 12.5 mm sapphire. Pump and probe pulses were polarized at the magic angle (54.7°) relative to each other. Laser pulse spot sizes (full-width-half-maximum) were 319.0 ± 1.2 µm for the 800 nm pump, 310.0 ± 22.7 µm for the 400 nm pump, and 118.0 ± 2.7 µm for the probe.

The signal was detected with a spectrograph (Newport, 77 400) and camera (Andor, Zyla sCMOS). TA measurements were taken with samples at 40 ppm in 2 mm path-length quartz cuvettes (Starna Cells, 21-Q-2) and samples were stirred continuously during the experiment. Minimal photodegradation was observed. Further details regarding the TA spectroscopy under photocatalytic conditions can be found in Section S5.5 (Supporting Information).

Transient Electrical Measurements: Photo-CELIV, transient photovoltage (TPV) and time-resolved charge extraction (TRCE) measurements were performed using the commercially available PAIOS 2 system (Fluxim AG). For carrier transport and charge extraction data, a light pulse from a white LED (Cree, xp-g) was used to generate charges, while a compensating offset voltage held the device at open circuit. The end of the light pulse was simultaneous with the application of either a linearly increasing voltage (20 mV s^{-1} to a maximum extraction voltage of −3 V) for photo-CELIV or square-step voltage (≈100 ns switching time from open to short circuit) for TRCE to extract photogenerated charges. The current transients were recorded by the integrated PAIOS hardware. For TPV measurements the device was held at open circuit under illumination via a compensating bias, then a small perturbation was created via a step-change increase in the illumination to induce a corresponding small increase in the V_{OC}. The small perturbation lifetime was determined by fitting the decay of the voltage back to steady state V_{OC} as the perturbation light change was removed as has been described previously.[61]

Supporting Information

Supporting Information is available from the Wiley Online Library or from the author.

Acknowledgements

A.D. and X.P. contributed equally to this work. The authors acknowledged the facilities, and the scientific and technical assistance of Microscopy Australia and the Australian National Fabrication Facility (ANFF) under the National Collaborative Research Infrastructure Strategy, at the South Australian Regional Facility, Flinders Microscopy and Microanalysis, Flinders University. Additionally, the authors appreciated the scientific and technical assistance of Microscopy Australia at the University of South Australia, a facility that is cofunded by the University of South Australia, the State and Federal Governments. The authors acknowledged Dr. Ashley Slattery and Adelaide Microscopy for assistance in the TEM experiments. A.D. and J.M.d.l.P. acknowledged support from the Australian Government Research Training Stipend. J.M.d.l.P. acknowledged a Playford Trust Ph.D. Scholarship, a Constance Fraser Supplementary Scholarship, and a Forrest George and Sandra Lynne Young Supplementary Scholarship. This work was supported by grants from the Australian Research Council (Nos. DP160103797, DP220102900, LE0989747, LE200100051, DP230102705, and FT230100154). A.S. and D.B. greatly acknowledged the photovoltaic fabrication and characterization facilities at King Abdullah University of Science and Technology (KAUST) Solar Center, and the support from KAUST Office of Sponsored Research (OSR) under Award No. OSR-2019-CARF/CCF-3079.

Open access publishing facilitated by Flinders University, as part of the Wiley - Flinders University agreement via the Council of Australian University Librarians.

Conflict of Interest

The authors declare no conflict of interest.

Data Availability Statement

The data that support the findings of this study are available from the corresponding author upon reasonable request.

Keywords

homojunction OPV, low-donor content, organic semiconductors, photocatalysis, photovoltaics, quantum mechanics, renewable energy

Received: September 19, 2023
Revised: December 14, 2023
Published online:

---

[1] G. Li, R. Zhu, Y. Yang, *Nat. Photonics* **2012**, *6*, 153.
[2] N. Espinosa, M. Hösel, D. Angmo, F. C. Krebs, *Energy Environ. Sci.* **2012**, *5*, 5117.
[3] Y. Wang, A. Vogel, M. Sachs, R. S. Sprick, L. Wilbraham, S. J. A. Moniz, R. Godin, M. A. Zwijnenburg, J. R. Durrant, A. I. Cooper, J. Tang, *Nat. Energy* **2019**, *4*, 746.
[4] M. Z. Rahman, M. G. Kibria, C. B. Mullins, *Chem. Soc. Rev.* **2020**, *49*, 1887.
[5] E. K. Solak, E. Irmak, *RSC Adv.* **2023**, *13*, 12244.
[6] S. Trasatti, *Pure Appl. Chem.* **1986**, *58*, 955.
[7] J. Wang, P. Xue, Y. Jiang, Y. Huo, X. Zhan, *Nat. Rev. Chem.* **2022**, *6*, 614.
[8] Y. Lin, J. Wang, Z.-G. Zhang, H. Bai, Y. Li, D. Zhu, X. Zhan, *Adv. Mater.* **2015**, *27*, 1170.
[9] C. Yan, S. Barlow, Z. Wang, H. Yan, A. K.-Y. Jen, S. R. Marder, X. Zhan, *Nat. Rev. Mater.* **2018**, *3*, 18003.
[10] Y. Shi, Y. Chang, K. Lu, Z. Chen, J. Zhang, Y. Yan, D. Qiu, Y. Liu, M. A. Adil, W. Ma, X. Hao, L. Zhu, Z. Wei, *Nat. Commun.* **2022**, *13*, 3256.
[11] J. Kosco, M. Bidwell, H. Cha, T. Martin, C. T. Howells, M. Sachs, D. H. Anjum, S. Gonzalez Lopez, L. Zou, A. Wadsworth, W. Zhang, L. Zhang, J. Tellam, R. Sougrat, F. Laquai, D. M. Delongchamp, J. R. Durrant, I. Mcculloch, *Nat. Mater.* **2020**, *19*, 559.
[12] J. Kosco, S. Gonzalez-Carrero, C. T. Howells, T. Fei, Y. Dong, R. Sougrat, G. T. Harrison, Y. Firdaus, R. Sheelamanthula, B. Purushothaman, F. Moruzzi, W. Xu, L. Zhao, A. Basu, S. De Wolf, T. D. Anthopoulos, J. R. Durrant, I. Mcculloch, *Nat. Energy* **2022**, *7*, 340.
[13] Y. Yang, D. Li, P. Wang, X. Zhang, H. Zhang, B. Du, C. Guo, T. Wang, D. Liu, *Polymer* **2022**, *244*, 124667.
[14] M. V. Pavliuk, S. Wrede, H. Tian, *Chem. Commun.* **2023**, *59*, 5611.
[15] H. Gao, C. Han, X. Wan, Y. Chen, *Ind. Chem. Mater.* **2023**, *1*, 60.
[16] J. M. De La Perrelle, A. Dolan, E. R. Milsom, T. D. Small, G. F. Metha, X. Pan, M. R. Andersson, D. M. Huang, T. W. Kee, *J. Phys. Chem. C* **2022**, *126*, 14518.
[17] A. Dolan, J. M. de la Perrelle, T. D. Small, E. R. Milsom, G. F. Metha, X. Pan, M. R. Andersson, D. M. Huang, T. W. Kee, *ACS Appl. Nano Mater.* **2022**, *5*, 12154.
[18] A. Brnovic, L. Hammarström, H. Tian, *J. Phys. Chem. C* **2023**, *127*, 12631.
[19] E. Gutierrez-Fernandez, A. D. Scaccabarozzi, A. Basu, E. Solano, T. D. Anthopoulos, J. Martín, *Adv. Sci.* **2021**, *9*, 2104977.
[20] M. B. Price, P. A. Hume, A. Ilina, I. Wagner, R. R. Tamming, K. E. Thorn, W. Jiao, A. Goldingay, P. J. Conaghan, G. Lakhwani, N. J. L. K. Davis, Y. Wang, P. Xue, H. Lu, K. Chen, X. Zhan, J. M. Hodgkiss, *Nat. Commun.* **2022**, *13*, 2827.
[21] Q. Guo, Q. Guo, Y. Geng, A. Tang, M. Zhang, M. Du, X. Sun, E. Zhou, *Mater. Chem. Front.* **2021**, *5*, 3257.
[22] N. Yao, J. Wang, Z. Chen, Q. Bian, Y. Xia, R. Zhang, J. Zhang, L. Qin, H. Zhu, Y. Zhang, F. Zhang, *J. Phys. Chem. Lett.* **2021**, *12*, 5039.
[23] Y. Wang, M. B. Price, R. S. Bobba, H. Lu, J. Xue, Y. Wang, M. Li, A. Ilina, P. A. Hume, B. Jia, T. Li, Y. Zhang, N. J. L. K. Davis, Z. Tang, W. Ma, Q. Qiao, J. M. Hodgkiss, X. Zhan, *Adv. Mater.* **2022**, *34*, 2206717.
[24] X. Pan, J. M. Bjuggren, M. Jevric, W. L. Tan, C. R. Mcneill, M. R. Andersson, *Chem. Mater.* **2022**, *34*, 5103.
[25] M. M. O'connor, T. J. Aubry, O. G. Reid, G. Rumbles, *Adv. Mater.* **2023**, 2210481.
[26] X. Wan, C. Li, M. Zhang, Y. Chen, *Chem. Soc. Rev.* **2020**, *49*, 2828.
[27] A. Sharma, S. Singh, X. Song, D. Rosas Villalva, J. Troughton, D. Corzo, L. Toppare, G. Gunbas, B. C. Schroeder, D. Baran, *Chem. Mater.* **2021**, *33*, 8602.
[28] E. Saglamkaya, A. Musiienko, M. S. Shadabroo, B. Sun, S. Chandrabose, O. Shargaieva, G. Lo Gerfo M, N. F. Van Hulst, S. Shoaee, *Mater. Horiz.* **2023**, *10*, 1825.
[29] N. Schopp, G. Akhtanova, P. Panoy, A. Arbuz, S. Chae, A. Yi, H. J. Kim, V. Promarak, T.-Q. Nguyen, V. V. Brus, *Adv. Mater.* **2022**, *34*, 2203796.
[30] Y. Firdaus, V. M. Le Corre, S. Karuthedath, W. Liu, A. Markina, W. Huang, S. Chattopadhyay, M. M. Nahid, M. I. Nugraha, Y. Lin, A. Seitkhan, A. Basu, W. Zhang, I. McCulloch, H. Ade, J. Labram, F. Laquai, D. Andrienko, L. J. A. Koster, T. D. Anthopoulos, *Nat. Commun.* **2020**, *11*, 5220.

[31] S. Zeiske, W. Li, P. Meredith, A. Armin, O. J. Sandberg, *Cell Rep. Phys. Sci.* **2022**, *3*, 101096.
[32] V. D. Mihailetchi, J. Wildeman, P. W. M. Blom, *Phys. Rev. Lett.* **2005**, *94*, 126602.
[33] P. Hartnagel, T. Kirchartz, *Adv. Theory Simul.* **2020**, *3*, 2000116.
[34] S. R. Cowan, A. Roy, A. J. Heeger, *Phys. Rev. B* **2010**, *82*, 245207.
[35] J. Vollbrecht, V. V. Brus, S.-J. Ko, J. Lee, A. Karki, D. X.i Cao, K. Cho, G. C. Bazan, T.-Q. Nguyen, *Adv. Energy Mater.* **2019**, *9*, 1901438.
[36] S. Ryu, N. Y. Ha, Y. H. Ahn, J.-Y. Park, S. Lee, *Sci. Rep.* **2021**, *11*, 16781.
[37] Q. Wang, K. Domen, *Chem. Rev.* **2019**, *120*, 919.
[38] D. Kroh, F. Eller, K. Schötz, S. Wedler, L. Perdigón-Toro, G. Freychet, Q. Wei, M. Dörr, D. Jones, Y. Zou, E. M. Herzig, D. Neher, A. Köhler, *Adv. Funct. Mater.* **2022**, *32*, 2205711.
[39] Y. Fu, T. H. Lee, Y.-C. Chin, R. A. Pacalaj, C. Labanti, S. Y. Park, Y. Dong, H. W. Cho, J. Y. Kim, D. Minami, J. R. Durrant, J.-S. Kim, *Nat. Commun.* **2023**, *14*, 1870.
[40] J. Fang, Z. Wang, Y. Chen, Q. Zhang, J. Zhang, L. Zhu, M. Zhang, Z. Cui, Z. Wei, H. Ade, C.-Q. Ma, *Cell Rep.* **2022**, *3*, 100983.
[41] A. Holmes, E. Deniau, C. Lartigau-Dagron, A. Bousquet, S. Chambon, N. P. Holmes, *ACS Nano* **2021**, *15*, 3927.
[42] K. N. Schwarz, S. B. Farley, T. A. Smith, K. P. Ghiggino, *Nanoscale* **2015**, *7*, 19899.
[43] G. Wen, R. Hu, X. Su, Z. Chen, C. Zhang, J. Peng, X. Zou, X. He, G. Dong, W. Zhang, *Dyes Pigm.* **2021**, *192*, 109431.
[44] X. Zou, G. Wen, R. Hu, G. Dong, C. Zhang, W. Zhang, H. Huang, W. Dang, *Molecules* **2020**, *25*, 4118.
[45] J. Yuan, Y. Zhang, L. Zhou, G. Zhang, H.-L. Yip, T.-K.i Lau, X. Lu, C. Zhu, H. Peng, P. A. Johnson, M. Leclerc, Y. Cao, J. Ulanski, Y. Li, Y. Zou, *Joule* **2019**, *3*, 1140.
[46] W. Zhu, A. P. Spencer, S. Mukherjee, J. M. Alzola, V. K. Sangwan, S. H. Amsterdam, S. M. Swick, L. O. Jones, M. C. Heiber, A. A. Herzing, G. Li, C. L. Stern, D. M. Delongchamp, K. L. Kohlstedt, M. C. Hersam, G. C. Schatz, M. R. Wasielewski, L. X. Chen, A. Facchetti, T. J. Marks, *J. Am. Chem. Soc.* **2020**, *142*, 14532.
[47] Z. Wang, K. Gao, Y. Kan, M. Zhang, C. Qiu, L. Zhu, Z. Zhao, X. Peng, W. Feng, Z. Qian, X. Gu, A. K.-Y. Jen, B. Z. Tang, Y. Cao, Y. Zhang, F. Liu, *Nat. Commun.* **2021**, *12*, 332.
[48] J. Xiao, X.' Jia, C. Duan, F. Huang, H.-L. Yip, Y. Cao, *Adv. Mater.* **2021**, *33*, 2008158.
[49] J. Yang, Y. Geng, J. Li, B. Zhao, Q. Guo, E. Zhou, *J. Phys. Chem. C* **2020**, *124*, 24616.
[50] K. Xian, Y. Liu, J. Liu, J. Yu, Y. Xing, Z. Peng, K. Zhou, M. Gao, W. Zhao, G. Lu, J. Zhang, J. Hou, Y. Geng, L. Ye, *J. Mater. Chem. A* **2022**, *10*, 3418.
[51] S.-I. Natsuda, T. Saito, R. Shirouchi, Y. Sakamoto, T. Takeyama, Y. Tamai, H. Ohkita, *Energy Environ. Sci.* **2022**, *15*, 1545.
[52] S.-I. Natsuda, Y. Sakamoto, T. Takeyama, R. Shirouchi, T. Saito, Y. Tamai, H. Ohkita, *J. Phys. Chem. C* **2021**, *125*, 20806.
[53] R. Wang, C. Zhang, Q. Li, Z. Zhang, X. Wang, M. Xiao, *J. Am. Chem. Soc.* **2020**, *142*, 12751.
[54] V. M. Le Corre, A. R. Chatri, N. Y. Doumon, L. J. A. Koster, *Adv. Energy Mater.* **2017**, *7*, 1701138.
[55] J. Lorrmann, B. H. Badada, O. Inganäs, V. Dyakonov, C. Deibel, *J. Appl. Phys.* **2010**, *108*, 113705.
[56] L. Zhu, J. Zhang, Y. Guo, C. Yang, Y. Yi, Z. Wei, *Angew. Chem., Int. Ed.* **2021**, *60*, 15348.
[57] M. Azzouzi, P. Calado, A. M. Telford, F. Eisner, X. Hou, T. Kirchartz, P. R. F. Barnes, J. Nelson, *Sol. RRL* **2020**, *4*, 1900581.
[58] O. J. Sandberg, K. Tvingstedt, P. Meredith, A. Armin, *J. Phys. Chem. C* **2019**, *123*, 14261.
[59] L. Krückemeier, Z. Liu, T. Kirchartz, U. Rau, *Adv. Mater.* **2023**, *35*, 2300872.
[60] S. Subianto, R. Balu, L. De Campo, A. Sokolova, N. K. Dutta, N. R. Choudhury, *ACS Appl. Mater. Interfaces* **2018**, *10*, 44116.
[61] B. C. O'regan, F. Lenzmann, *J. Phys. Chem. B* **2004**, *108*, 4342.